NAVAL POSTGRADUATE SCHOOL

MONTEREY, CALIFORNIA

THESIS

USING DESIGN-BUILD-TEST CYCLES TO DEMONSTRATE FREE UUV PROPULSION IN A KARMAN VORTEX STREET USING A FLEXIBLE BODY

by

Devon L. Florendo

December 2023

Thesis Advisor: Joseph T. Klamo
Second Reader: Fotis A. Papoulias

THIS PAGE INTENTIONALLY LEFT BLANK

REPORT DOCUMENTATION PAGE	*Form Approved OMB No. 0704-0188*

1. AGENCY USE ONLY ***(Leave blank)***	**2. REPORT DATE** December 2023	**3. REPORT TYPE AND DATES COVERED** Master's thesis

4. TITLE AND SUBTITLE
USING DESIGN-BUILD-TEST CYCLES TO DEMONSTRATE FREE UUV PROPULSION IN A KARMAN VORTEX STREET USING A FLEXIBLE BODY

5. FUNDING NUMBERS
ONR Code 32;
JON R4KU

6. AUTHOR(S) Devon L. Florendo

7. PERFORMING ORGANIZATION NAME(S) AND ADDRESS(ES)
Naval Postgraduate School
Monterey, CA 93943-5000

8. PERFORMING ORGANIZATION REPORT NUMBER

9. SPONSORING / MONITORING AGENCY NAME(S) AND ADDRESS(ES)
Office of Naval Research, One Liberty Center, 875 N. Randolph Street, Suite 1425, Arlington, VA 22203-1995

10. SPONSORING / MONITORING AGENCY REPORT NUMBER

11. SUPPLEMENTARY NOTES The views expressed in this thesis are those of the author and do not reflect the official policy or position of the Department of Defense or the U.S. Government.

12a. DISTRIBUTION / AVAILABILITY STATEMENT
Approved for public release. Distribution is unlimited.

12b. DISTRIBUTION CODE
A

13. ABSTRACT (maximum 200 words)

This thesis explored the possibility of a flexible synthetic body undergoing passive synchronization with a von Kármán wake to generate propulsive thrust without expending any energy. The experiments conducted for this thesis were performed in a recirculating water tunnel and used flexible synthetic bodies made from Ecoflex 00–10 silicone rubber. Calibration of the water tunnel and a load cell used for force measurements were performed prior to testing. The research effort completed five design-build-test cycles. The iterative cycles demonstrated a quick and inexpensive fabrication process, showed that the silicone rubber material used had sufficient flexibility to synchronize, discovered that direct interaction between the flexible body and passing vortices is not able to produce flapping motion in the synthetic body, and suggested that the rotation of the front portion of the body is a key factor for passive wake synchronization and thrust generation to occur. Any role that lateral translation of the body plays in the synchronization process still needs to be explored in future efforts.

14. SUBJECT TERMS
passive propulsion, Kármán vortex street

15. NUMBER OF PAGES
81

16. PRICE CODE

17. SECURITY CLASSIFICATION OF REPORT	**18. SECURITY CLASSIFICATION OF THIS PAGE**	**19. SECURITY CLASSIFICATION OF ABSTRACT**	**20. LIMITATION OF ABSTRACT**
Unclassified	Unclassified	Unclassified	UU

NSN 7540-01-280-5500

Standard Form 298 (Rev. 2-89)
Prescribed by ANSI Std. 239-18

THIS PAGE INTENTIONALLY LEFT BLANK

Approved for public release. Distribution is unlimited.

USING DESIGN-BUILD-TEST CYCLES TO DEMONSTRATE FREE UUV PROPULSION IN A KARMAN VORTEX STREET USING A FLEXIBLE BODY

Devon L. Florendo
Lieutenant, United States Navy
BS, Virginia Military Institute, 2016

Submitted in partial fulfillment of the
requirements for the degree of

MASTER OF SCIENCE IN SYSTEMS ENGINEERING

from the

NAVAL POSTGRADUATE SCHOOL
December 2023

Approved by: Joseph T. Klamo
Advisor

Fotis A. Papoulias
Second Reader

Oleg A. Yakimenko
Chair, Department of Systems Engineering

THIS PAGE INTENTIONALLY LEFT BLANK

ABSTRACT

This thesis explored the possibility of a flexible synthetic body undergoing passive synchronization with a von Kármán wake to generate propulsive thrust without expending any energy. The experiments conducted for this thesis were performed in a recirculating water tunnel and used flexible synthetic bodies made from Ecoflex 00–10 silicone rubber. Calibration of the water tunnel and a load cell used for force measurements were performed prior to testing. The research effort completed five design-build-test cycles. The iterative cycles demonstrated a quick and inexpensive fabrication process, showed that the silicone rubber material used had sufficient flexibility to synchronize, discovered that direct interaction between the flexible body and passing vortices is not able to produce flapping motion in the synthetic body, and suggested that the rotation of the front portion of the body is a key factor for passive wake synchronization and thrust generation to occur. Any role that lateral translation of the body plays in the synchronization process still needs to be explored in future efforts.

THIS PAGE INTENTIONALLY LEFT BLANK

Table of Contents

List of Figures

List of Tables

THIS PAGE INTENTIONALLY LEFT BLANK

List of Acronyms and Abbreviations

.STL	Stereo lithography
CAD	computer-aided design
CI	confidence interval
DAQ	Data Acquisition
DOD	Department of Defense
FDM	fused deposition modeling
NI	National Instruments
NPS	Naval Postgraduate School
PC	polycarbonate
UT	ultrasonic transducer
UUV	Unmanned underwater vehicle
VIVACE	Vortex-Induced Vibrations Aquatic Clean Energy
VIV	vortex-induced vibrations

THIS PAGE INTENTIONALLY LEFT BLANK

Executive Summary

This thesis explored the possibility of creating passive propulsion, previously observed for a euthanized trout in a vortex wake, using a synthetic flexible body. One consideration was the size and strength of the von Kármán vortex street, which can be changed experimentally by varying the size of cylinder used to create the vortices and the speed of the incoming fluid. The other consideration was the properties of the flexible synthetic body such as the length, width, height, and elasticity needed to generate passive thrust while within the von Kármán vortex street. Once the influence these factors have on the synthetic body's interaction with the vortex wake are understood, they can be used to optimize designs of unmanned underwater vehicles (UUV) to allow for the ability to generate propulsive thrust without expending any energy.

This research effort utilized various pieces of equipment. An Eidetics Flow Visualization Water Tunnel Model 1520 located at NPS was used to test flexible synthetic bodies interacting with a von Kármán vortex street. Three different test setups were used to experimentally test the flexible bodies. One setup involved having the flexible bodies rigidly attached to a load cell to measure forces on the body produced by the interaction with passing vortices. The second test setup attached the flexible bodies to a stepper motor to force flexible body motion. The third setup involved having the flexible bodies tethered to the vortex generating cylinder. Molds for the flexible bodies were created through 3D printing using a Fortus 450mc 3D printer. The silicone rubber used to create the bodies was Ecoflex 00-10 product.

Before testing the synthetic bodies in the water tunnel, verification of the equipment was performed. A calibration of the water tunnel was completed to characterize its performance. This allowed the tunnel operator to set the water depth and motor frequency to obtain the desired tunnel speed during testing. An AMTI strain gauge load cell was calibrated to verify the sensitivity and accuracy when measuring the small expected loads on the flexible body during testing. Data collection equipment included both an ultrasonic transducer (UT) sensor and the load cell, while video collection was performed with a Dual Pixel 12.0 MP camera.

The research completed five design-build-test cycles. The first cycle focused on the devel-

opment of a fabrication method to create synthetic bodies using silicone rubber and the verification that the created body had the necessary flexibility. The second cycle improved the fabrication process and attempted to increase the interaction between the flexible body and the passing vortices. The third cycle looked at generating rotation in the forward part of the body to cause a traveling wave to move down the flexible body and create flapping motion. The fourth cycle utilized a stepper motor to introduce forced sinusoidal rotations at the front of the flexible body to create flapping motion in the aft portion of the body. The fifth cycle aimed to create a tethered body that had all six degrees-of-freedom of motion within the water tunnel while eliminating sources of friction in previous iterations.

After completing the five design-build-test cycles, the following lessons learned were identified. The silicone rubber material used provided the required body flexibility to produce a flapping motion. The fabrication process developed for generating flexible bodies for this effort was quick and inexpensive. The direct interactions between the flexible bodies and the passing vortices was not able to produce flapping motion in the synthetic body. The rotation of the head of the flexible body is a key factor for generating flapping motion within a vortex wake. Future research can focus on designing and using a nearly friction-free rotation system, introducing lateral translation for the flexible body, and improving the free floating synthetic body design.

CHAPTER 1:
Introduction

1.1 Motivation

Unmanned underwater vehicles (UUVs) are increasingly important for Department of Defense (DOD) strategy involving missions that include intelligence, surveillance, reconnaissance, mine countermeasures, tactical oceanography, communications, navigation, and anti-submarine warfare [1]. There is a trend in UUV design to require more energy as their missions become longer in duration and involve more sensors for information gathering and communications. The operational capabilities of UUVs when deployed is affected by the amount of energy the batteries in the vehicle can store. This is because batteries are a finite energy source that creates limitations on mission duration, range, and speed. To combat the growing demands for more energy, UUV size has increased to provide more internal volume to house more batteries. Currently, UUV sizes can reach up to 9071 kg (20, 000 lbs) of displacement with a diameter of 91.44 cm (36 in) [2].

The increase in size of UUVs to fulfill mission needs creates a transportation issue for UUV operations. UUVs normally transit themselves from a deployment point to the mission area. However, they still need to be hauled from their home port to the deployment point though either transportation on a ship, which takes up valuable cargo space, or transiting themselves, which uses up a portion of their limited battery energy. This research proposes a way for UUVs to transit from the pier to the deployment point using little to no energy. This would both free up valuable cargo space on transport ships and eliminate UUV energy usage during the transit to the deployment point. Furthermore, this would remove the consideration of limited cargo space on ships as a consideration during UUV design.

1.2 Application

The reduction in UUV energy usage while transiting would be accomplished by utilizing the previously observed fact that a flexible body is able to passively extract energy from a vortical wake and convert it into thrust. A transport ship could be modified to create a vortex

wake which the UUVs would then utilize to achieve energy-free propulsion. The transport ship would create the vortex wake by towing a bluff object such as a vertical D-shaped cylinder as used in this research.

Figure 1.1 shows a schematic of the proposed application. The transport ship is shown towing D-shaped cylinders creating a vortex wake with flexible UUVs within the wake.

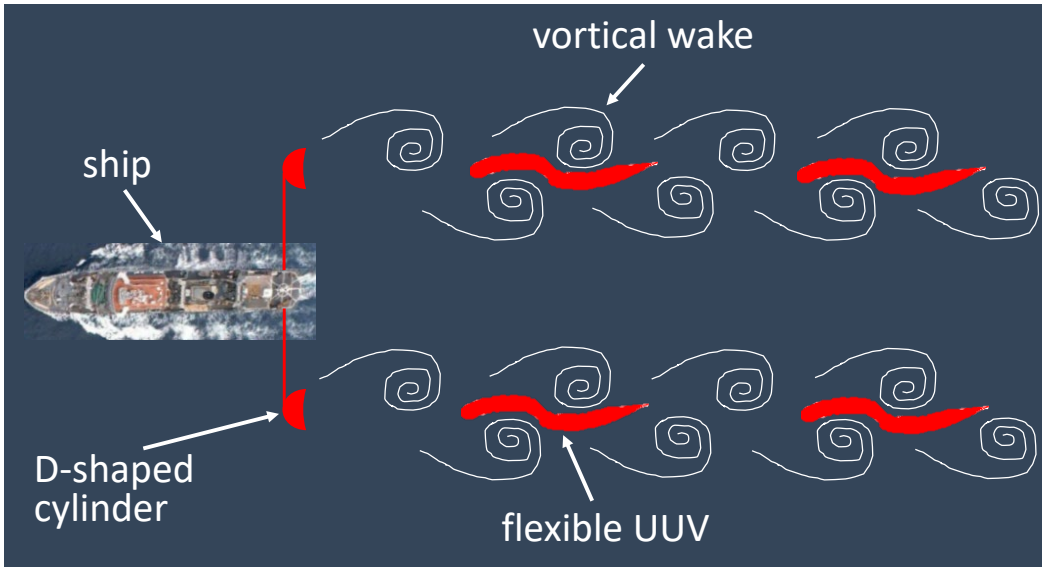

Figure 1.1. A ship towing a bluff object to create a vortex wake which UUVs are able to extract energy from for propulsion.

This method could be expanded through the towing of multiple bluff objects on either side of the ship to create multiple vortex wakes. Additionally, having multiple flexible bodies, in-line with each other utilizing the same vortex wake, might be possible as well. This approach may be dependent on the strength of the shed vortices and have limits to the number of UUVs that can be involved. This is because as the distance downstream from the bluff object increases the strength of the vortices decreases limiting the vortices' ability to influence the UUV. Also, each successive UUV that interacts with a propagating vortex also wakens it. Utilizing this method of UUV transportation would improve transportation efficiency. While a ship towing the D-cylinder would marginally decrease its own performance, due to

the increased drag it must overcome caused by the cylinder in the water, this is outweighed by the cargo space that would now be available. Also, the UUV performance would be improved by conserving the finite energy onboard for future operations.

1.3 Background

Fluid passing by a fixed bluff object sheds vortices into the flow at a certain frequency. This frequency is known as the Strouhal frequency and is part of the nondimensional shedding parameter called the Strouhal number [3]. The Strouhal number is dependent on the Reynolds number of the flow. The Reynolds number is a nondimensional velocity and is defined as the ratio of inertial force to the viscous force [4]. When a bluff object oscillates at certain amplitudes and frequencies, the shedding frequency can be altered so that it no longer equals the Strouhal frequency. The shedding frequency of the vortices then matches the oscillation frequency of the bluff object.

Wake synchronization is when an object's oscillation frequency matches the incoming vortices or the vortices it produces in its wake. Wake synchronization can be achieved by two different methods: active or passive. Active synchronization is where the object itself is forced to oscillate at a given amplitude and frequency to achieve synchronization with its own wake. An example of active synchronization would be oscillating a cylinder in a fluid stream to increase the heat transfer or mixing within the fluid by increasing the shedding frequency. Alternatively, passive synchronization occurs when incoming fluid vortices cause the body to oscillate at a certain frequency. In many cases passive synchronization occurs at the natural frequency of the body. An example of passive synchronization is vortex-induced vibrations (VIV), which is observed when a bluff body interacts with fluid flow and begins to oscillate which can cause fatigue failure. VIV occurs in structures such as heat exchanger tube bundles, marine structures, bridges, and power transmission lines [5].

Passive synchronization is a vital consideration for system design. The possible danger that exists if passive synchronization is not considered was highlighted by the structural failure of the Tacoma Narrows bridge. The Tacoma Narrows bridge failed due to the torsion oscillation caused by large scale vortices both above and below the roadway [6]. Conversely, harnessing passive synchronization can positively impact a system by extracting energy from a fluid. The Vortex-Induced Vibrations Aquatic Clean Energy (VIVACE) system is a device

that utilizes VIV to extract clean and renewable energy from river, ocean, and other water resources [7].

The principle of active and passive synchronization has been observed in fish for the purpose of generating thrust. A fish uses active synchronization while swimming through a vortical flow to exploit vortices to reduce the energy needed for locomotion [8]. Taking this principle, a step further, a euthanized trout exposed to a vortex wake achieved passive synchronization to propel itself forward through the water [9]. This phenomenon demonstrated the possibility of a flexible body utilizing a vortex wake to generate thrust without expending any energy. Figure 1.2 shows six still frame images of the euthanized trout with a line denoting the location of the front of the fish on the first frame. The subsequent frames show the fish moves forward as time increases. This demonstrated the ability of passive synchronization to produce thrust in a flexible body.

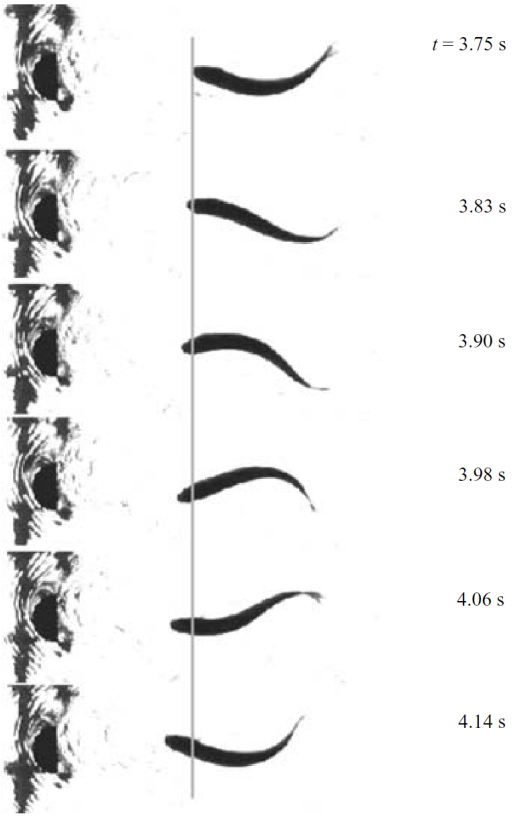

Figure 1.2. The vortices convecting downstream in the fluid induce a flapping motion in the dead trout's body which generates thrust from the resultant tail motion, accelerating the body forward against its own drag. Source: [9].

Beal et al. [9] explored the passive synchronization phenomenon displayed by the euthanized trout. A high-aspect-ratio foil was used in place of the euthanized trout to show the possibility of mechanical extraction of energy from the vortex wake [9]. However, this demonstration did not parameterize the elements required to recreate the passive synchronization. Additionally, the shift to a foil did not explore various body types which might be able to achieve passive synchronization. This could have been achieved through repeating the demonstration with the euthanized trout for various fish species.

The body structure of a fish is complex and not likely to be duplicated as a UUV. Therefore, the extraction of energy from a vortex wake would only be useful if it can be accomplished using simpler synthetic bodies. An attempt to recreate passive synchronization using a syn-

thetic body was previously attempted using silicone rubber molds of trout. The experiment conducted by Toming et al. [10] was fundamentally different from those conducted by Beal et al. The synthetic fish was rigidly attached to a testing fixture rod at a fixed distance behind a D-shaped cylinder and it had no degrees-of-freedom. In contrast, the fish in Beal et al. was completely free in all six degrees-of-freedom limited only by a string attaching it to the D-shaped cylinder. Figure 1.3 shows a picture of the Toming et al. test set up. The D-shaped cylinder is on the left with the synthetic fish attached to the force plate with a rigid rod on the right. The synthetic fish is positioned at a distance of three diameters downstream from the D-shaped cylinder.

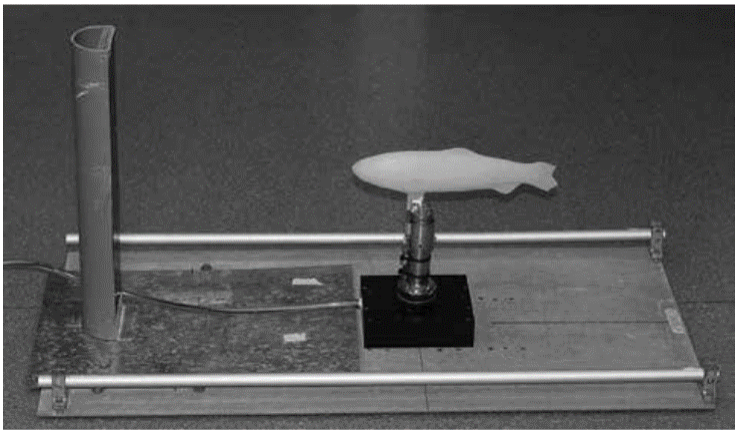

Figure 1.3. A photo showing the experimental setup to Toming et al. in which a silicone rubber fish was fixed with a rigid rod to the force plate, at a distance of three diameters downstream from the D-shaped cylinder. Source: [10].

The degrees-of-freedom that the synthetic body lacks is not the only consideration. The actual rigidity, or flexibility, of the synthetic body itself is another consideration when comparing both experiments. The synthetic body was created using platinum cured silicon rubber Dragon Skin R10 from SMOOTH-ON Inc with a shore hardness of 10A. These differences of mounting and materials resulted in the synthetic fish acting like a rigid body.

1.4 Methodology

This research utilized repeated design-build-test cycles which leverage an iterative process to understand flexible body passive synchronization and attempt to fabricate bodies that are able to achieve energy-free propulsion. The design phase consisted of utilizing the solid modeling computer-aided design (CAD) software SolidWorks to design molds to create the synthetic bodies and adapters, which were used to attach the bodies to the testing rig. The build phase involved the creation of the molds and adapters via 3D printing before and then the curing a silicone body within the printed parts. The created silicone rubber bodies were placed into a water tunnel to measure the loads on it using a load cell and filmed to record body motion during the test phase. The design-build-test cycle was then repeated utilizing the lessons learned to apply to the next cycle.

THIS PAGE INTENTIONALLY LEFT BLANK

CHAPTER 2:
Facility and Equipment

2.1 Water Tunnel

This investigation used an Eidetics model 1520 free surface recirculating water tunnel located at Naval Postgraduate School (NPS). The facility has a test section that is 38.1 cm wide, 50.8 cm deep, and 152.4 cm long (15 in x 20 in x 60 in). Figure 2.1 shows the water tunnel with the test section and part of the settling chamber visible.

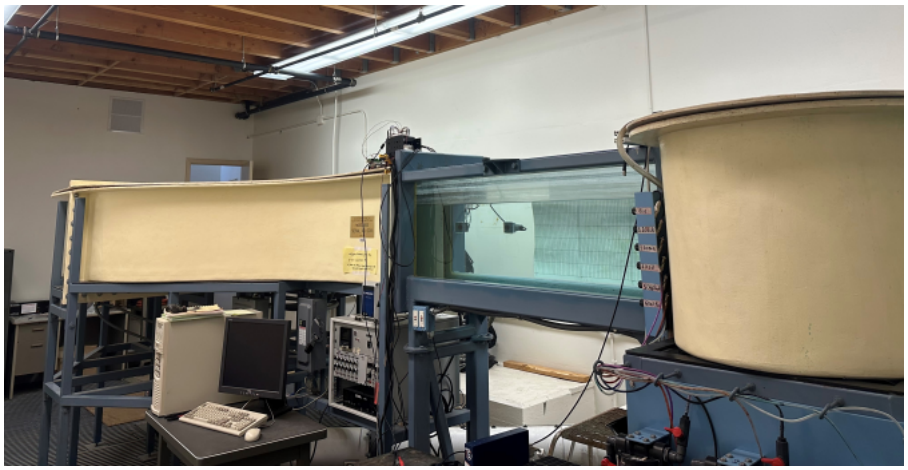

Figure 2.1. Image of the Eidetics model 1520 recirculating water tunnel at NPS.

The dimensions of the water tunnel limit the size of the flexible bodies used for testing due to blockage effects and the fact that the walls of the tunnel can suppress vortices generated by a cylinder that is too close to the walls [11]. The blockage ratio is the profile area of the object in the test section divided by the cross sectional area of the test section itself [12]. Ideally, the blockage ratio should be less than 5 percent [13], but at least less than 10 percent, to minimize effects on the shedding frequency and characteristics of the vortex wake [11].

The cross sectional area of this water tunnel is 1935.49 cm^2, which for a 5 percent blockage ratio a test body maximum area is 96.774 cm^2.

The speed of the tunnel is adjusted by setting the angular frequency of the tunnel motor over a range from 2 Hz to 40 Hz. The water depth in the test section affects the realized fluid speed in the test section since the pump moves a constant volume of water. The corresponding fluid speed in the test section for a water depth of 35.6 cm (14 in), which was used for this research, translates to 0.013 m/s (0.043 ft/sec) to 0.479 m/s (1.572 ft/sec) over the mentioned motor frequency range.

The water tunnel is equipped with a Dynasonics Series TFX ultrasonic transducer (UT) sensor for measuring the water tunnel speed in the test section. The sensor works by having two transducers that can send and receive sound waves. The water speed is determined by measuring the time it takes for the sound wave to travel between the transducers [14]. Due to the location of the UT sensor, the minimum water depth in the test section was restricted to 27.9 cm (11 in) to be able to collect tunnel speed measurements. Since the UT sensor was mounted in the front portion of the test section, the flexible body was placed in the back portion so it would not interfere with the sensor operation.

2.2 Testing Setups

The research effort used three different test setups to study flexible body passive synchronization. All setups utilized 80/20 aluminum T-slot bars to create a frame which was positioned over the top of the test section and used to attach the required testing equipment. The frame was secured to the top of the water tunnel utilizing C-clamps. The T-slot frame design enabled a large amount of freedom when positioning the equipment both vertically and horizontally within the water tunnel test section. The difference between the three test setups was the number of degrees-of-freedom motion that the flexible body mounting adapter had in the water tunnel.

The first setup restricted the mounting adapter to zero degrees-of-freedom. Figure 2.2 shows this test setup along with the important components annotated.

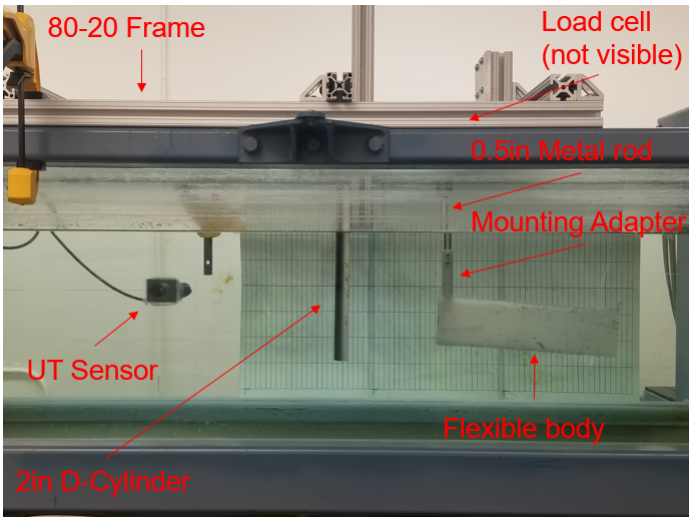

Figure 2.2. Annotated image of the load cell variant test setup with flexible body attached.

A load cell was attached to the 80/20 frame using an L-bracket. To connect the flexible body to the load cell a 1.27 cm (0.5 in) diameter rod was attached to the bottom side of the load cell using a coupling. A 3D printed adapter was embedded in the front part of the flexible body and was attached to this rod with two 1/4-20 bolts and nuts. This held the front of the flexible body fixed and allowed for the measurement of the forces and moments on the body. A 5.08-cm (2-in) diameter D-shaped cylinder was placed in front of the flexible body and used to generate the vortical wake. This cylinder's total surface area is 526.98 cm^2 with a height of 30.48cm (12-in), exceeding the ideal blockage ratio. The D-cylinder and flexible body were attached to two separate cross-beams which provided the ability to set any desired separation distance between the D-cylinder and flexible body. The separation distance was set to 15.2 cm (6 in), or three-cylinder diameters, apart to avoid the suction zone directly behind the D-cylinder. The height of the D-cylinder and the flexible body were set to keep any 80/20 parts used in the test setup out of the water to minimize disturbances in the fluid flow.

The research used an AMTI MC3A load cell with a 3-axis strain gauge and 100-lbs capacity to measure hydrodynamic loads on the flexible body. The load cell captured forces and

moments in the x, y, and z axes as shown in Figure 2.3.

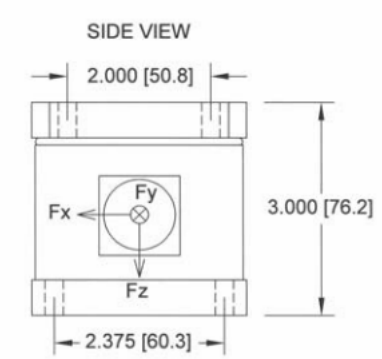

Figure 2.3. AMTI MC3A load cell side profile displaying axis orientation and dimensions in inches and [mm]. Source: [15]

The load cell coordinate system follows the right-hand rule and the load cell was positioned in the tunnel such that the positive x-axis was aligned directly opposite the direction of flow in the test section. This would display any drag forces as a negative number and any thrust produced as a positive number. The positive y-axis was toward the left side of the body when looking forward from behind the body and the positive z-axis was pointed upward opposite the direction of gravity. Table 2.1 summarizes the settings used for the AMTI MC3A Load cell during testing.

Table 2.1. AMTI MC3A load cell settings used during testing.

Load	F_x (lbs)	F_y (lbs)	F_z (lbs)	M_x (in-lbs)	M_y (in-lbs)	M_z (in-lbs)
Range	±10.00	±10.00	±20.83	±33.33	±33.33	±20.00
Analog sensitivity	500 (mV/lb)	500 (mV/lb)	240 (mV/lb)	150 (mV/in-lb)	150 (mV/in-lb)	250 (mV/in-lb)

In addition to setting the analog sensitivity, the voltage excitation and zero setpoint for each channel were also set to 10.0 V and 0% respectfully. The load cell is capable of measuring forces along the x-axis from 0lbs to 50lbs with a sensitivity of μ V/V-lbs for the F_x axis [15].

The second test setup allowed for the mounting adapter to have one rotational degree of freedom about the vertical axis. The AMTI MC3A load cell was replaced by a NEMA 17 stepper motor, model number 17HM19-1684D-E1000. When the stepper motor was not energized, the shaft was free to rotate with a minimum amount of internal friction resisting the motion. This allowed for the ability of the forward portion of the flexible body to rotate. Additionally, the stepper motor could be energized to force rotational motion of the mounting adapter, and thus the front portion of the flexible body, to actively create the flapping motion. This motor has a step angle of 0.9 degrees, equaling 400 steps per revolution. The stepper motor was controlled with an Arduino microprocessor that outputs signals to a model DM542T stepper motor driver manufactured by Leadshine. The Arduino was powered by a model LRS-50-5 5V power supply manufactured by Mean Well USA Inc. The stepper motor was powered by a model LRS-150-24 24V power supply manufactured by Mean Well USA Inc as well.

The last test setup consisted of connecting the flexible body directly to the D-shaped cylinder with fishing line. To accomplish this an eyebolt was screwed into the front of flexible body at the midplane. The fishing line was secured to the D-cylinder using a Trucker's Hitch knot and the eye bolt was tied off with an improved clinch knot with a length of 15.2 cm (6 in) to match the downstream distance of the other two test setups. To stabilize the body when it was attached to the D-cylinder, numerous 0.8 g and 0.7 g round lead split shot weights were clamped onto the bottom of the body using pliers which could be removed if necessary.

During testing, the analog voltages from the six load cell channels and the UT sensor were collected by a National Instruments (NI) USB-6363 16 channel X Series Data Acquisition (DAQ) device. This device performed the analog to digital conversion at a sampling rate of 25 Hz. This data was saved to a computer via USB as ASCII files using a custom-written script in MATLAB.

2.3 Silicone Rubber

The silicon rubber used for this research was Platinum cured silicone rubber Ecoflex 00-10 from SMOOTH-ON Inc. Typically, differences in silicone material is captured using a shore hardness scale. Shore hardness is the measure of the resistance of a material to indentation, which is divided into three different scales 00, A, and D as shown in Figure 2.4 [16].

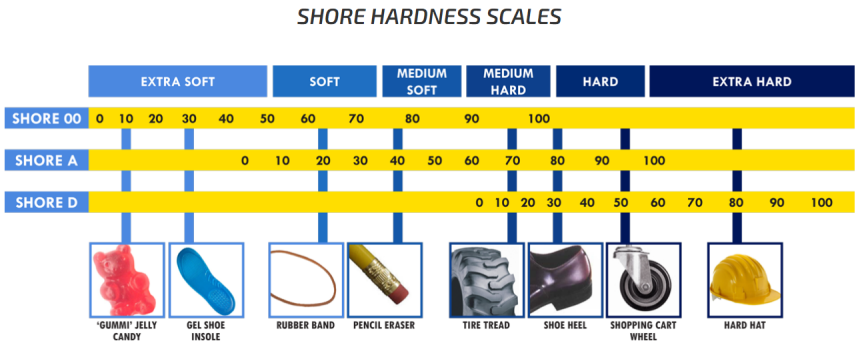

Figure 2.4. Shore hardness scales with example materials. Source: [16]

The Ecoflex 00-10 product has a shore hardness of 10 using the 00 scale. This silicone is softer compared to the Dragon Skin R10 used by Toming et al. that had a shore hardness of 10 using the A scale. Shore hardness is related to Young's Modulus which is used to capture a material's ability to stretch, thus the material can also be considered more flexible.

The flexible body creation process using Ecoflex 00-10 followed the manufacturer's instructions. The product comes in two separate containers labeled Parts A and Parts B. The parts are measured and pre-mixed separately. Both parts would then be mixed at a volume ratio of 1:1 for at least 3 minutes and left to begin the curing process. The time for mold curing was a minimum of 4 hours when at room temperature. Additionally, the Ease Release^{TM} 200 release agent from SMOOTH-ON Inc. was applied to the mold before pouring in the silicone rubber to ensure the flexible body was able to be easily removed when fully cured [17].

2.4 3D Printing

This research utilized a Fortus 450mc 3D printer for creating all the molds and adapters that were used during testing. The material used for 3D printing was a polycarbonate (PC) filament from Stratasys. The 3D printer employs fused deposition modeling (FDM) for additive manufacturing using the PC filament to specifications based on the uploaded Stereo lithography (.STL) file. Since the surface finish of the printed parts was not critical, no post-processing of the printed pieces was done. The .STL files for each part were created

using the 3D computer-aided design (CAD) software SolidWorks. All 3D printed parts fit within the machine envelope of 406.4 mm by 355.6 mm by 406.4 mm (16 in x 14 in x 16 in) and were printed as single pieces [18].

THIS PAGE INTENTIONALLY LEFT BLANK

CHAPTER 3:
Procedures

3.1 Water Tunnel Calibration

The UT sensor was configured to provide two output signals. One output signal was sent to an auxiliary computer running Dynasonics software and displayed the average speed of the water tunnel on the computer monitor. The second output signal was routed to the NI DAQ which sampled the analog voltage output. A calibration of the water tunnel UT sensor was conducted to enable converting the recorded analog voltage tunnel speed signal to a speed in physical units instead. The measured analog voltage was matched to the average speed provided by the Dynasonics software, to create a calibration curve that related the measured UT sensor voltage to tunnel speed.

The calibration was conducted over various motor frequencies and water heights to fully characterize the tunnel's performance. The water heights considered were 43.18 cm (17 in), 35.56 cm (14 in) and 27.94 cm (11 in) to verify the mass flow rate of the motor remained nearly constant regardless of the water depth. A constant mass flow rate would mean that decreasing the height of the water would increase the test section speed for a fixed motor frequency. The motor frequency range used was 2 Hz to 40 Hz, where 2 Hz was the minimum commanded speed to begin motion of the motor shaft and above 40 Hz risked tripping the circuit breaker to the motor due to the large current draw. Increments of 0.5 Hz were used when running the motor between 2 Hz to 5 Hz and increments of 2.5 Hz were used when running between 5 Hz and 40 Hz. Figure 3.1 contains the collected calibration data along with uncertainty bars, the linear regression line, and the confidence interval (CI) on the regression line.

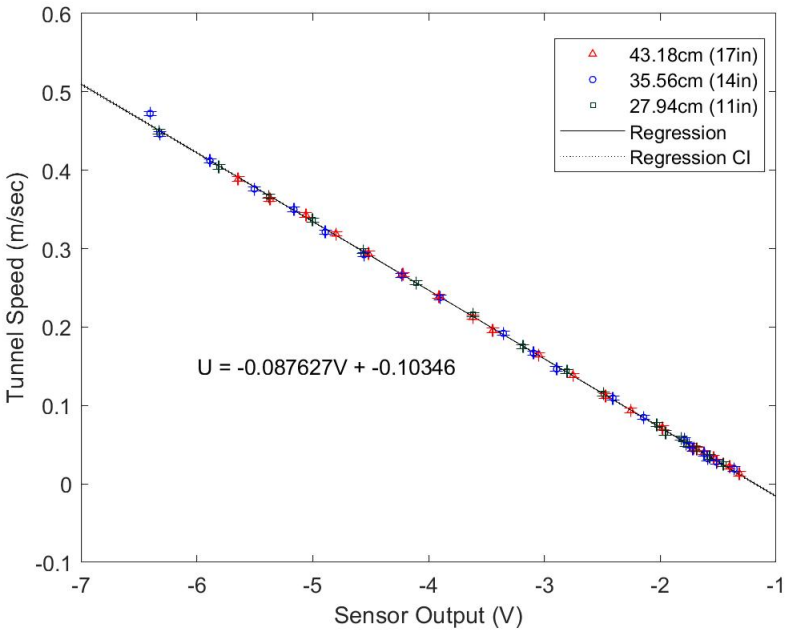

Figure 3.1. Linear regression result for water tunnel speed as a function of UT sensor voltage with confidence interval and error bars.

The figure shows data taken with a water depth of 43.18 cm (17 in) in red, a water depth of 35.56 cm (14 in) in blue, and a water depth of 27.94 cm (11 in) in green. The vertical error bars display an uncertainty of ±0.0006 m/s (±0.002 ft/s) which is based on observing the fluctuations of the average speed displayed by the Dynasonics software. The horizontal error bars display an uncertainty of ±0.0028V which is based on the standard error from the regression calculation. The CI of the regression line is so small that the CI bounds cannot be discerned from the regression line itself in the figure. The regression fit of the collected data shows a linear relationship that is captured mathematically as

$$U = -0.087627(V + 1.180686) \tag{3.1}$$

where U is the tunnel speed in meters per second and V is the UT sensor output signal in volts. The equation of the regression line was put it into a form consisting of a "gain" and an

"offset" term. During testing, equation 3.1 was utilized to convert the collected UT sensor output voltage data into tunnel speed. This provided a better estimate of the tunnel speed than using the tunnel speed reading from the Dynasonics software.

This research effort also included a second analysis that related the motor angular frequency to the achieved tunnel speed in the test section as a function of water height. To perform this analysis, the motor angular frequency, which had also been manually recorded for each run, was also included. This allowed the relationship between motor angular frequency and tunnel speed to be determined. However, the relationship between the tunnel speed and a given motor frequency will be dependent on the water depth in the test section. The same water tunnel calibration data set that was used for the first analysis was used here to determine the required motor frequency for a desired tunnel speed given the water height in the test section. Figure 3.2 presents the effects that the water depth has on the achieved tunnel speed in the test section for a given motor angular frequency.

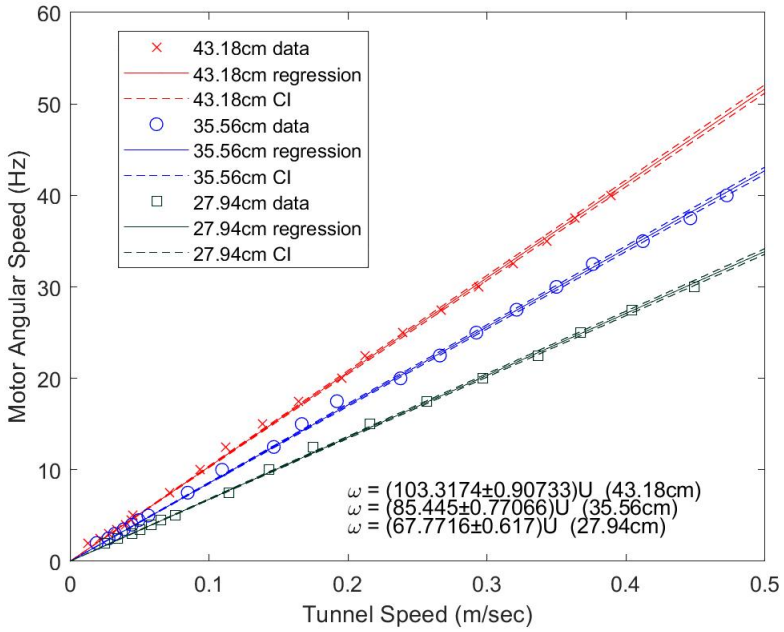

Figure 3.2. Linear regression results for the motor angular frequency as a function of water tunnel speed for three different water heights.

This dependence on water height is shown by the increase in the slope of each regression line as the water height increases. Essentially the motor angular frequency must increase to achieve the same fluid speed in the test section as the water depth increases. This behavior is consistent with the hypothesis that the motor moves a nearly constant mass of water at a fixed angular frequency regardless of the water depth. Using dimensional analysis, the mathematical expression

$$\dot{m}[\mathrm{kg/s}] = \psi[\mathrm{kg/rev}]\,\omega[\mathrm{rev/s}] = \rho[\mathrm{kg/m^3}]\,U[\mathrm{m/s}]\,w[\mathrm{m}]\,h[\mathrm{m}] \tag{3.2}$$

can be formed where $\dot{m}$ is the mass flow rate, ψ is the mass of water moved each motor revolution, ω is the motor angular frequency, ρ is the water density, w is the width of the test section, and h is the water depth.

Equation 3.2 can be rearranged to identify the parameters that make up the slope of the regression line that captures the relationship between the motor angular frequency and the tunnel speed shown in Figure 3.2. This results in

$$\omega = \left(\frac{\rho w h}{\psi}\right) U = CU \tag{3.3}$$

where $C = (\rho w/\psi)h$ and its value was determined by the regression coefficients in Figure 3.2, one for each water depth. These values can be used to determine the value of the $\rho w/\psi$ component of the expression in parenthesis. Figure 3.3 shows the linear regression coefficients from Figure 3.2 plotted against the water depth. The coefficient of this linear regression is the value of $\rho w/\psi$.

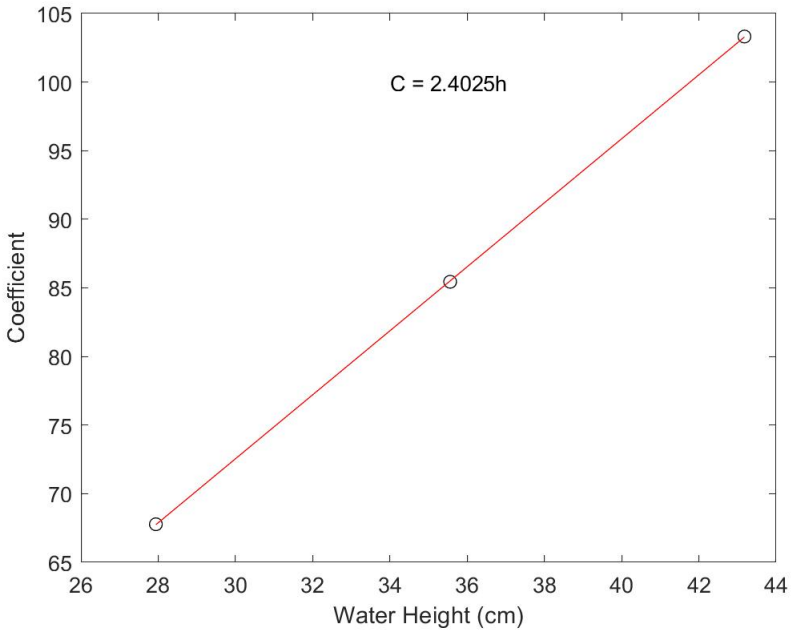

Figure 3.3. Motor frequency for a desired tunnel speed given the height.

Using these results, Equation 3.3 can be updated as follows

$$\omega = 2.4025\, h\, U \tag{3.4}$$

which allows a tunnel operator to determine the motor angular frequency to set to achieve a desired water speed in the test section for any water depth. The required motor angular frequency is simply the product of the desired fluid velocity, in meters per seconds, the water depth, in centimeters, and 2.4025.

3.2 Load Cell Calibration

A calibration of the load cell was conducted to confirm the manufacturer's provided gain values for each channel and to ensure the load cell had adequate sensitivity to measure the small loads experienced by the flexible bodies subjected to the fluid velocities used during this research. The calibration was conducted on the two axes that measured the drag and

lateral side force on the flexible bodies during testing. The vertical axis was not calibrated because of the minimal expected forces along that axis during testing. The calibration was performed by rotating the load cell as necessary to be able to hang known weights from the load cell along each of the two axes of interest, one at a time. The test weights used ranged from 0.2224 N (0.05 lbs) to 13.345 N (3 lbs) with increments of 0.2224 N (0.05 lbs) from 0.2224 N (0.05 lbs) to 2.224 N (0.5 lbs) and increments of 2.224 N (0.5 lbs) from 2.224 N (0.5 lbs) to 13.345 N (3 lbs). During the calibration, a random order was used when hanging the weights from the load cell to minimize sensor hysteresis. The range of 0.2224 N (0.05 lbs) to 2.224 N (0.5 lbs) was used to prove that the load cell configured with our particular settings had sufficient accuracy to measure the expected loads. The range of 2.224 N (0.5 lbs) to 13.345 N (3 lbs) was used to verify the full range of functionality of the load cell. The applied forces from the applied weights were compared to the measured values as shown in Figure 3.4. Table A.1 and Table A.2 contain all values used for the load cell calibration in the appendix.

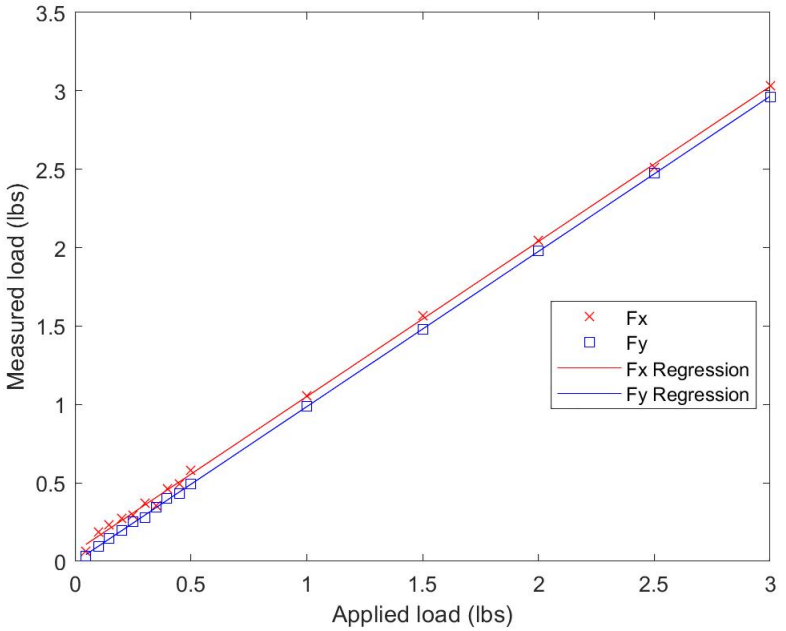

Figure 3.4. Load cell calibration results showing the applied and measured forces.

In Figure 3.4 the load cell x-axis results are shown as the red cross data points while the load cell y-axis results are represented as the blue square data points. A linear regression line was also calculated and displayed in the figure. The results demonstrated that the force measurements of the load cell are sensitive enough to determine discrete changes in the drag force and lateral side force on the flexible body. The expected drag force on the flexible body was expected to be quite small due to the D-cylinder interrupting the fluid flow onto the body due to the vortex wake it created.

3.3 Data Collection Procedure

During testing of the flexible bodies, UT sensor and load cell voltage data was collected. The data collection process was completed using the following procedure:

1. Place test setup on top of the water tunnel and secure it with clamps
2. Connect the load cell cables and turn on the signal conditioner to start the load cell warm-up process which lasts for 30 min
3. Connect the flexible body to the test setup using 1/4-20 bolts
4. Flip on water tunnel circuit breaker
5. Turn on UT sensor main power supply
6. Turn on the NI USB-6363 DAQ
7. Turn on UT sensor auxiliary computer
8. Turn on data collection laptop containing MATLAB
9. Set MATLAB data collection parameters (run number, run length, and sampling frequency)
10. Take a zero run to remove sensor offsets
11. Turn on the motor and set motor frequency to achieve the desired tunnel speed and verify stable tunnel speed on the auxiliary computer
12. Collect data at 25Hz sampling rate for one minute
13. Repeat steps 11 and 12 until all desired data is collected

3.4 Video Collection and Processing

This research also collected video data to capture body motion. Video data was collected using a Samsung Galaxy 8 with a Dual Pixel 12.0 MP camera. During video data collection,

the camera was handheld except for when viewing the flexible body from below and space was limited underneath the water tunnel. In that situation, the camera was placed on a flat surface centered below the water tunnel and positioned looking up to have the proper field of view. Videos of the flexible body were taken from the left side of the test section looking at the body, from behind the body looking forward, and from below the body looking up. Video collection duration varied from 15 sec to 30 sec.

During testing when using the stepper motor to force body rotation, the body motion was quantified by tracking high-contrast points along the bottom of the body. The flexible body was marked with black dots along the centerline of the bottom of the body. The top of the tank was covered with white poster board to create a featureless white background that provided high contrast compared to the black dots. The video was then processed in MATLAB to isolate the dots on the body from the surrounding environment utilizing the contrast of the black dots and the white background. The video was converted to black and white color values to simplify the thresholding process. The value of the black dots was determined to be any pixel with a value less than 145. A filter was applied to each frame of the video, which took any pixel value above 145 and set it to 255 to isolate the black dots and show body motion. The pixel location of the black dots over time could then be determined if desired.

CHAPTER 4:
Design - Build - Test Cycles

4.1 Cycle 1 - Solve Body Fabrication Issues

4.1.1 Goals

The first cycle focused on the creation of a fabrication method for flexible bodies, the verification of adequate silicone rubber flexibility, and the exploration of the flexible body's interaction with the vortex wake. The first goal was to demonstrate a fabrication method for a flexible body that includes an embedded adapter to attach a body to the test setup. Challenges for this goal included selecting a single piece or two piece mold design, along with an integrated way to position the adapter during the curing process. Once the flexible body was constructed the next goal was to prove that the silicone rubber had sufficient flexibility to produce oscillatory flapping motion. If the body was deemed to have sufficient flexibility the next goal was to observe the amount of interaction between the flexible body and the vortex wake. The difficulty with getting the first body to interact with the vortex wake is that multiple variables potentially play a role in producing the flapping motion. Such variables include the tunnel speed and the separation distance between the flexible body and the upstream vortex wake generator. These parameters require a iterative testing approach to determine whether each one has a positive or negative effect on producing a flapping motion from the flexible body.

4.1.2 Design

The design phase started with the need to decide on using a single piece or two piece mold design. The benefit of a single piece mold design is that it eliminates the possibility of any silicone leaking out during curing, which promotes a consistent curing process. A single piece mold design however creates the complication of having to extract the flexible body from the mold without being able to open it. A single piece design raises the possibility of damaging the body during removal. On the other hand, a two piece design does not introduce the same risk to the body during extraction since the mold is made to be disassembled and

opened to expose the flexible body. The seam created from a two piece design however could allow for leakage during curing. This can be mitigated through the use of tape along the seam. Another consideration is that even if leakage is prevented, the seam where the two mold pieces meet would introduce a ridge on the flexible body that would have to removed. Both one- and two-piece designs would also have to consider ways to minimize printing volume to minimize the overall time required to fabricate the mold. One way to reduce the amount of material required is to reduce the need for support structures. Any type of overhang in the design would require support material, thus increasing the amount of material used. Another way to reduce the amount of material required is to specify an infill setting value less than the solid fill value. Using infill creates a mold with internal gaps based on the selected pattern and percentage value. The percentage determines how compact the pattern is, with a higher percentage number filling the structure more completely. Infill settings used in this project were the standard setting for the Fortus 450mc 3D Printer which is 18 percent infill with a 1.524 mm (0.06 in) wall thickness.

4.1.3 Build

This build cycle accomplished the goal of creating a fabrication process to produce a flexible body, however, there were some difficulties that could be improved upon in future design-build-test cycle iterations. The flexible body created during this cycle is shown in Figure 4.1. The corresponding engineering drawings for the mold and adapter are shown in Figure A.1 and Figure A.2, respectively, in the appendix.

Figure 4.1. Cycle 1 pennant shaped flexible body with "L" shaped adapter.

The thickness used for the mold walls allowed for deformation in the overall shape of the mold. The strategy for securing both pieces of the mold together during the curing process could also be improved. The clamps were insufficient to prevent leakage through the mold seam along the length of the body. This leakage during the curing process resulted in the body height being only 7.62 cm (3 in) instead of the expected 15.24 cm (6 in). Another issue was due to the additive manufacturing process of 3D printing, which created rough surface finishes. The rough surfaces made sealing the seam for a two piece mold design difficult. The solution to this issue was smoothing the surfaces by manually sanding them with sand paper.

4.1.4 Test

The key lessons learned from this design cycle pertained to the fabrication process, material flexibility, and body motion. During this cycle it was found that the silicone rubber used was sufficient to provide the required body flexibility. For this body, when holding the adapter, the flexible body collapsed completely under its own weight and hung straight down vertically. Demonstrating that the material was sufficient to produce a very small radius of curvature was important since it is required for the flapping motion. The flexible body was put into the water tunnel with the D-shaped cylinder upstream to generate a vortex wake. The interactions between the flexible body and the vortices are shown in Figure 4.2. The left photo shows the tail in its most extreme displacement in one direction while the right photo show the most extreme displacement in the other direction. The three photos in the figure show the flexible body responding to passing vortices however the overall displacement of the tail is rather small.

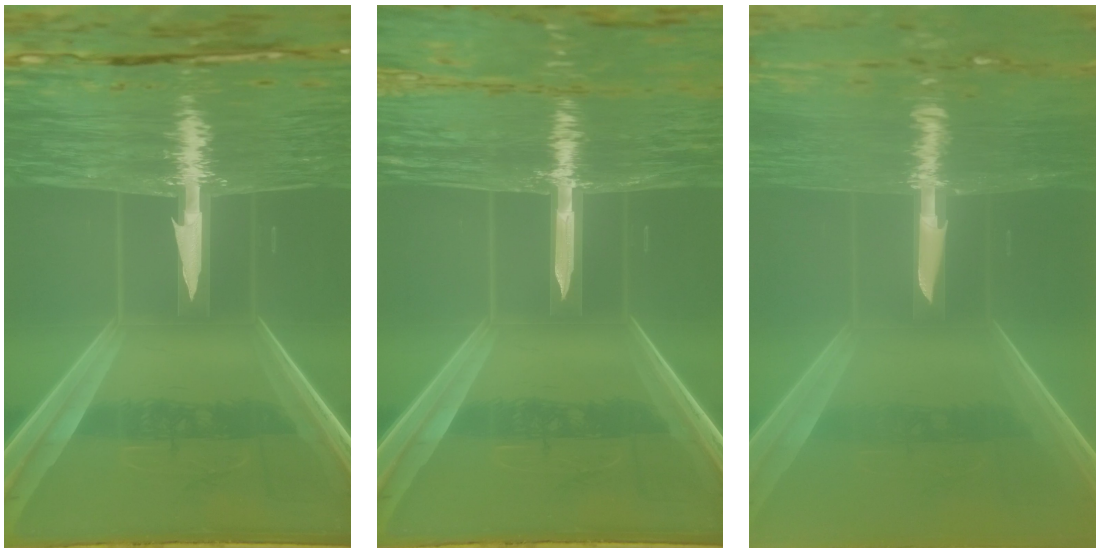

Figure 4.2. Cycle 1 flexible body motion due to vortex wake interaction for a flow speed of 0.47244 m/s (1.55 ft/s) with motor set to 40 Hz. The view is from the back of the water tunnel forwarding at the back of the flexible body.

The body's interactions with the vortices did not produce a significant flapping motion, rather the flexible body fluttered back and forth, which was most prevalent in the tail. The

motor was set to its highest setting of 40 Hz, which generated a speed in the test section of 0.47244 m/s (1.55 ft/s), to have the largest strength vortices possible. To promote stronger interactions between the flexible body and the vortices, the effects of increasing the body width were explored next.

4.2 Cycle 2 - Increasing Fluid Interactions

4.2.1 Goals

The second cycle focused on improving the fabrication process and increasing the direct fluid interaction between the body and the passing vortices. The first goal to improve the fabrication process centered around preventing mold deformation and silicone rubber leakage during curing. In this cycle the method of securing the two piece mold together was changed and the mold wall thickness was increased to prevent deformation. The second goal of improve body motion through direct fluid interaction was promoted by increasing the body width.

4.2.2 Design

This design phase addressed the goal of improving the fabrication process by stopping leakage and mold deformation during the curing process which was observed during the previous cycle. The mold deformation was eliminated by increasing the width of the mold design to 8.255 cm (3.25 in) and the wall thickness to 1.905 cm (0.75 in) while still using a low infill setting to minimize material usage. The increase in mold size and wall thickness improved the mold stability and also allowed for a better method of securing the two pieces together by applying more pressure which created a better seal. In this iteration the mold pieces were secured together with $1/4 - 20$ bolts and nuts, rather than clamps, to create a better seal. These changes can be seen in the engineering drawing of Figure A.3 in the appendix. Additionally, tape was applied along the seam of the mold during the curing process to ensure no leakage due to imperfection along the seam from the printing process occurred.

4.2.3 Build

This build cycle accomplished the goal of improving the fabrication process to produce the flexible body. The approach to embedding the adapter remained the same as the previous cycle. The flexible body created during this cycle is shown in Figure 4.3.

Figure 4.3. Cycle 2 4.445 cm (1.75 in) wide flexible body with "L" shaped adapter.

The modifications made to the body during this cycle were a reduction in length and an increase in the width. Since the separation distance, λ, between co-rotating pairs of shed vortices is given by

$$\lambda = \frac{D}{St} = \frac{5.08}{0.21} \approx 24.19\,\text{cm} \tag{4.1}$$

the length of the body was reduced to 25.4 cm (10 in) to limit the potential interaction to

only two vortexes at a time. The increased width of body, to 4.445 cm (1.75 in) wide, was to promote stronger direct fluid interactions by having more of the body in the path of the passing vortices. The width of the body did not taper in this iteration to allow for the entire body length to be closer to the central core of the shed vortices, also to promote stronger direct interaction. The body produced with the updated fabrication process was sufficient to address all fabrication concerns from the first cycle and thus all subsequent bodies were made using this approach.

4.2.4 Test

After observing the body interactions with the shed vortices in the water tunnel, the key lesson gathered during this design cycle was that direct fluid interaction alone does not generate enough side force on the aft section of the body to create a sufficiently large flapping motion. The interaction produced a very small swaying motion side the side rather than the fluttering observed in the previous cycle as shown in Figure 4.4.

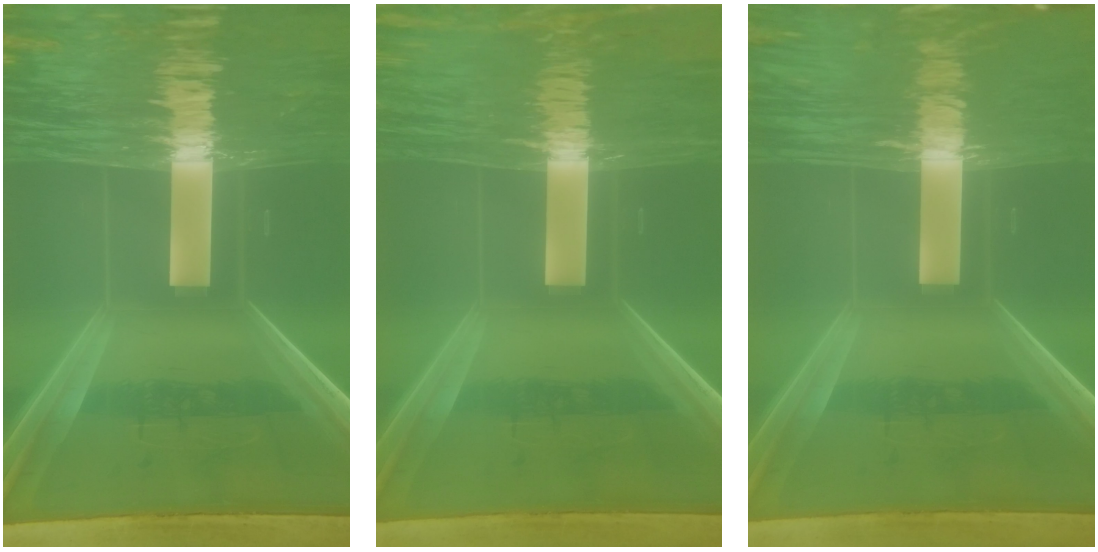

Figure 4.4. Cycle 2 flexible body motion due to vortex wake interaction for a flow speed of 0.47244 m/s (1.55 ft/s) with motor set to 40 Hz. The view is from the back of the water tunnel looking forward at the back of the flexible body.

Testing confirmed that direct vortex forcing was insufficient to produce a flapping motion

in the tail of the flexible body. This could be due to a number of reasons including the strength of the vortices were dissipating too much as they traveled down the length of the body, the generated pressure gradient across the two sides of the body was too small, or that direct vortex forcing on the tail is not the mechanism for producing the flapping motion previously observed. The observed small body motions and re-evaluation of the MIT euthanized fish experiments lead to a new hypothesis that significant flapping motion of the body is created by the flexible body's response to rotation of the forward portion of the body. The interaction of the vortices over the front portion of the body causes the head to rotate in the MIT experiments. This movement then travels down the length of the body due to the minimal rigidity that it has. Essentially, the body is rigid enough so that the aft portion of the body moves in response to the front moving but flexible enough so that the response is delayed and produces a flapping motion instead of rigid body motion.

4.3 Cycle 3 - Internal and External Means of Passive Body Rotation

4.3.1 Goals

The third cycle focused on generating rotation in the forward part of the body, referred to as the head, to cause a traveling wave to move down the length of the flexible body and create a flapping motion. This cycle includes three versions of different attachment approaches to the test setup to allow head rotation to the flexible body. The first version involved creating a new adapter design embedded in the flexible body that allowed for the body to rotate relative to the adapter. This was referred to as the internal rotational adapter since the relative motion occurred internal to the flexible body. This was accomplished by having the adapter be axially symmetric without any indentations to resist the relative motion between the adapter and flexible body as seen in the engineering drawing of Figure A.5 in the appendix.

The second version consisted of a different insert that was created specifically to be placed in between the adapter and the metal rod attached to the load cell to allow 1-degree of freedom rotation, typically referred to as yaw, about the head. This was referred to as the external rotational insert since the relative motion occurred external to the flexible body. The engineering drawings of Figure A.6 and A.7 in the appendix show the two different

attempts at this design version. To avoid having to reproduce additional bodies of identical design, the insert was created to be placed in between the existing adapter and metal rod designs. This allowed us to retest all previous bodies with the new rotational inserts.

The final version involved replacing the load cell with a de-energized stepper motor to reduce the overall friction of the components that were rotating relative to each other. The coupling on the shaft of the stepper motor was sized for a 1.27 cm (0.5 in) rod so the previously used rod that was attached to the load cell could now be attached to the stepper motor instead.

4.3.2 Design

The body shape used for this cycle of testing was tapered in the aft portion of the body. The body tapered to 2.54 cm (1 in) from the midpoint of the body rather than starting at the head. This change to the body design can be viewed in the engineering drawing of Figure A.4 in the appendix.

4.3.3 Build

A photo of the flexible body created during this cycle is shown Figure 4.5. Once the body was cured the adapter was rotated within the body by hand to ensure that the body would be able to rotate about the adapter if sufficient torque was provided.

Figure 4.5. Cycle 3 flexible body with internal rotational adapter. Notice that the "L"-shaped portion of the adapter, as seen in Figure 4.1, has been removed.

4.3.4 Test - Internal Rotational Adapter

The version one design explored the possibility of achieving head rotation by having the silicone rubber body itself rotate relative to the fixed adapted using an updated design. The adapter design was changed from an "L" shape to a circular, axis-symmetric one to allow for the possibility of head rotation. Also as part of this design, it was determined that the $1/4 - 20$ bolts connecting the adapter to the load cell, when the body was made to the expected 15.24 cm (6 in) height, would be submerged in the fluid and could create a wake. Therefore, the adapter was raised by 3.81 cm (1.5 in) to ensure that the bolts were completely out of the water. This was done by increasing the height of the notches that hold

the adapter in place during curing. The body width was maintained at 4.445 cm (1.75 in) to promote interaction with the vortices at the head of the body. After beginning to test this design in the water tunnel it became apparent that the internal friction was too large and head rotation would not occur. The flexible body exhibited similar swaying motion to the previous cycle as shown in Figure 4.6.

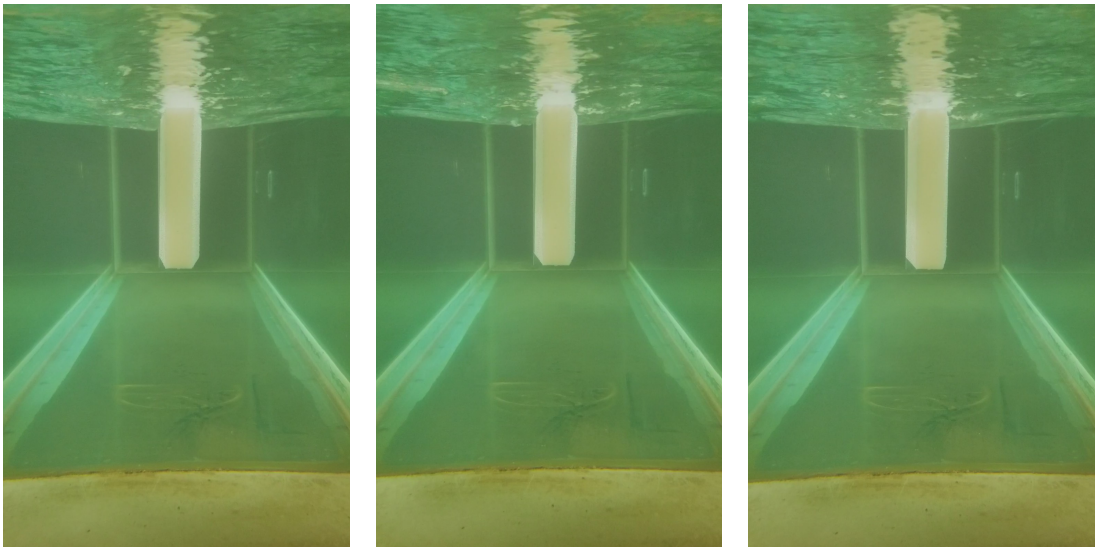

Figure 4.6. Cycle 3 flexible body motion due to vortex wake interaction for a flow speed of 0.47244 m/s (1.55 ft/s) with motor set to 40 Hz. The view is from the back of the water tunnel looking forward at the back of the flexible body.

Although the new circular adapter was able to be twisted relative to the flexible body by hand, the internal friction that had to be overcome would not allow for rotation by direct interaction with the vortex wake. Therefore, an external means would need to be explored in order to add the required degree-of-freedom to the body.

4.3.5 Test - External Rotational Insert

The external rotational approach involved the creation of an insert between the load cell metal rod and the body adapter. This insert would have a cavity in which dowels would rest in the $1/4 - 20$ bolt holes of the adapter instead of bolts. The insert would also maintain the $1/4 - 20$ bolt connection to the metal rod. This arrangement eliminated translational

motion between the metal rod and adapter in the vertical direction but allowed for rotation about the metal rod. The insert required significant space to minimize friction with the cavity surfaces. The insert can be viewed in the engineering drawing of Figure A.6 in the appendix.

This particular insert was not tested in a vortical wake in the water tunnel since the flexible body had a severe cant. The cavity was too large and this caused the flexible body to twist and introduced a severe cant as soon as the test set-up was placed in the test section of the water tunnel. The cant created by the external rotational insert is shown in Figure 4.7.

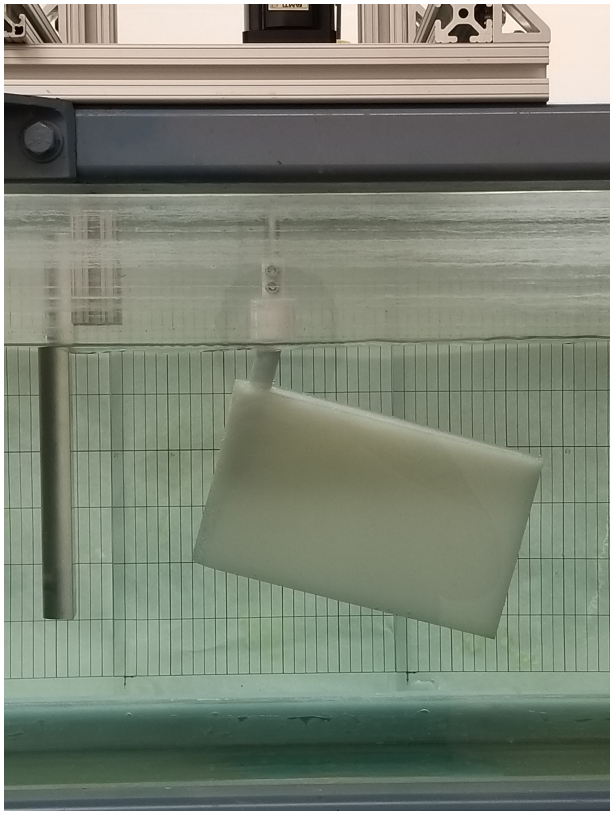

Figure 4.7. Severe cant caused by the initial external rotational insert.

Another iteration was made with an updated version of the insert. This updated version was designed to remove any body cant from the previous design. The updated insert design reduced the cavity tolerances and added area at the top of the cavity to keep the body from canting. The engineering drawing of the updated insert can be viewed in Figure A.7 in the

appendix. A flexible body connected to the test setup with the updated external rotational insert is shown in Figure 4.8.

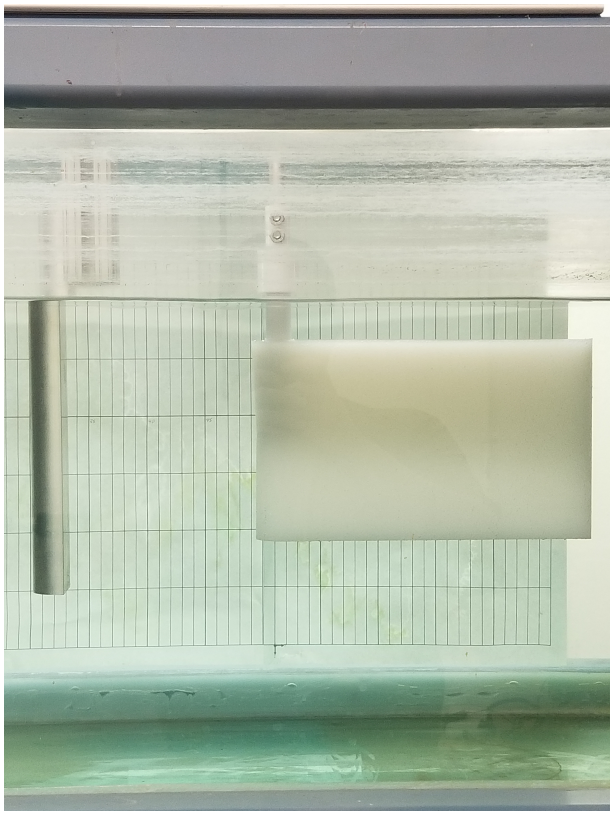

Figure 4.8. Updated external rotational insert design that fixed the previous cant problem.

The updated external rotational design was placed in the water tunnel for testing to see if the vortical wake could cause head rotation of the flexible body. During testing it was observed that, like with the internal rotational design, the passing vortices could not rotate the head of the body. This was still the case even though this external rotational design could be rotated much easier by hand compared to the internal rotational design. It was concluded that the PC filament used for the insert still introduced too much friction which prevented head movement from direct fluid forcing of the vortex wake.

4.3.6 Test - De-energized Stepper Motor

The next attempt adjusted the test setup to allow for yaw rotation while trying to further decrease friction effects through use of a bearing system. The test set-up was changed from using a load cell with a rotational insert to a de-energized stepper motor. The de-energized stepper motor acted like a low-friction rotating shaft due to the internal bearings of the stepper motor. The aim of this set-up was to reduce the rotational friction to a small enough level that the external fluid forcing on the flexible body could overcome it and rotate the head. The stepper motor when it was not energized does not provide any resistance to shaft rotation, however there still exists some internal friction in the bearings.

During testing in the water tunnel, this setup once again showed that the internal friction was too high to allow head rotation through interaction with the passing vortices. Therefore, different methods of securing the body while allowing for passive rotation would need to be used. One such method to create a near frictionless test setup would involving using air bearings with compressed air.

4.4 Cycle 4 - Stepper Motor Forced Rotation

4.4.1 Goals

The previous cycle showed that rotational friction was too large to be overcome by the vortical wake for all the various designs explored. Instead, this cycle utilized the energized stepper motor to introduce simple sinusoidal rotations to the head of the flexible body to see if this would create flapping motion at the tail. Furthermore, the research looked to determine if this flapping motion could impart momentum into the wake. This would then prove that if the rotational friction observed in the previous designs could be severely reduced or eliminated so that rotational motion of the head would occur, then that would create flapping motion in the tail of the flexible body and generate thrust.

4.4.2 Design

The body used for this cycle was shortened to a similar length of the trout used by Beal et al. previously. This was done to eliminate any possible effects that size variation has on generating flapping motion so that just the effects of rotation could be explored. The

updated body was 17.78 cm (7 in) long, 7.62 cm (3 in) tall and had a width of 2.54 cm (1 in) which tapered down to 0.635 cm (0.25 in). The adapter design was changed to include indentations that allowed silicone rubber to cure in between the indentations to prevent unwanted relative twisting between the adapter and the flexible body during the forced rotational motion. These changes can be viewed in the engineering drawings of Figure A.8 and Figure A.9 in the appendix.

4.4.3 Build

The flexible body created during this cycle is shown Figure 4.9. The entrained air within the silicone did create tiny pockets of air at the bottom of the adapter, but did not impact the flexibility of the body. Dots were then marked on the bottom of the body to track the motion during the forced rotations.

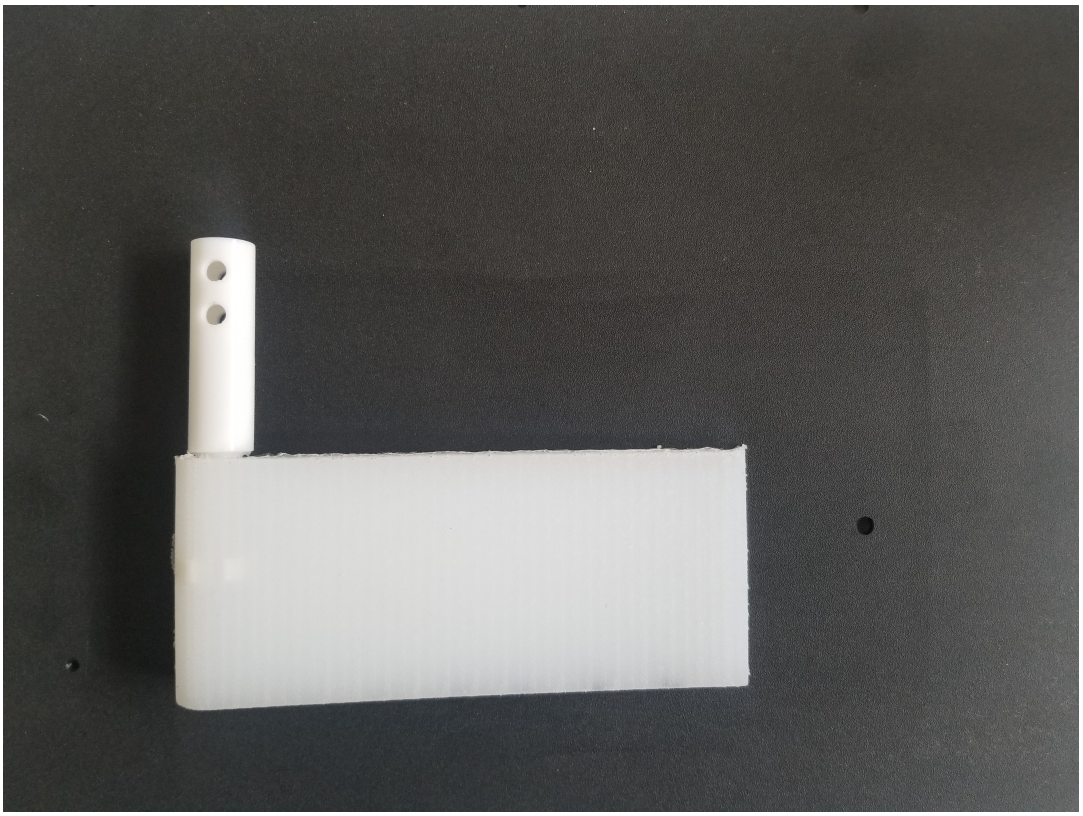

Figure 4.9. Cycle 4 stepper motor forced rotation flexible body with propeller adapter

4.4.4 Test

The stepper motor was commanded to produce back-and-forth rotations of its shaft covering a motion range of 90 degrees. The stepper motor motion starting from a 45 degree offset from the neutral position of the shaft. During testing, the production of thrust generated from the flapping body was assessed using of a 0.635 cm (0.25 in) thick aluminum plate that was attached to a set of parallel rails using four pillow block bearings. The plate was free to move along the rails which were aligned with the flow direction of the test section. The stepper motor was connected to this plate. Therefore, if the flapping body generated sufficient thrust, that force would be transferred through the test set-up and cause the plate

to move along the rails toward the front of the test section. The motion produced by the forced rotation of the flexible body head is shown in Figure 4.10(a) with Figure 4.10(b) the isolation of the dots marked on the bottom of the body.

(a) flexible body forced motion raw data

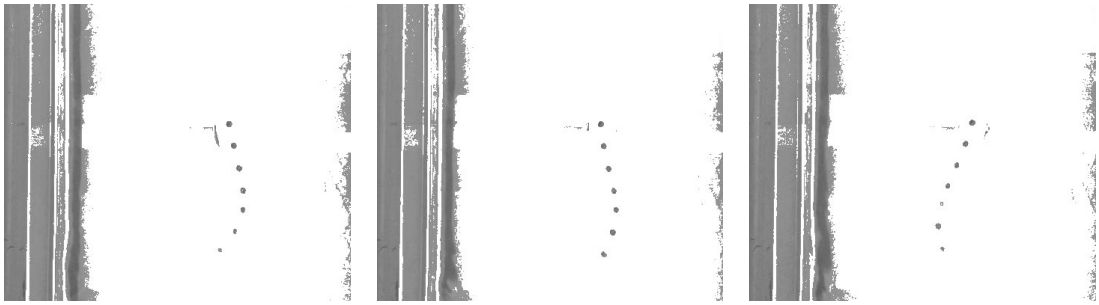

(b) flexible body forced motion with tracking points isolated

Figure 4.10. Cycle 4 stepper motor forced rotation of the flexible body looking up from below the water tunnel at the bottom of the flexible body

This cycle showed that head movement appears to be the key to producing the needed flapping movement of the flexible body. During continuous stepper motor forced rotations, it was observed that fluid interacting with the walls of the tank downstream suggested that the body was imparting momentum, at least transversely, to the fluid. However, this momentum was either not in the longitudinal direction or not large enough in magnitude to move the plate along the rails. The testing results also suggest that the body design used in this cycle might require optimization to maximize thrust as it was unable to push the plate forward.

4.5 Cycle 5 - Free Floating Body

4.5.1 Goals

The final iteration cycle of this research effort looked to eliminate all the attachments used to fix the flexible body to the test set-up. This would allow the elimination of all the various frictional forces that had potentially stopped the head rotation motion from occurring in the flexible body in previous cycles. Therefore, this cycle aimed to create a body that had all six degrees-of-freedom of motion within the water tunnel test section. The only attachment to the flexible body is a thin tether string connected from the D-cylinder to the front of the flexible body so that the body cannot be carried downstream by the flow and away from the cylinder. However, the set-up does allow for the flexible body to move upstream toward the D-cylinder. The major objective of the body design for this cycle was to create a shape that was stable within a vortex wake. If that was possible, then the secondary objective was to have the vortex wake create a flapping motion within the flexible body.

4.5.2 Design

This body had a vertical plane of symmetry and the overall body size returned to similar dimensions to that used for previous bodies to support a direct comparison. The body was 25.4 cm (10 in) long, had a maximum height of 15.24 cm (6 in) tall, tapered to a minimum height of 2.54 cm (1 in) at the back of the body, and had a width of 4.445 cm (1.75 in) which tapered to 2.54 cm (1 in). The purpose of tapering both height and width dimensions was to support the eventual attachment of a solid rigid fin structure to the body if it was able to first stabilize within the vortex wake. The mold design was adjusted to allow for filling the mold from the tail end of the body. The engineering drawings of the mold can be viewed in Figure A.10 in the appendix.

4.5.3 Build

The flexible body created during this cycle is shown in Figure 4.11. Once the body fully cured, an eyebolt was screwed into the front of the body to serve as the attachment point for the tether string. Fishing line was used to connect to the D-cylinder to eyebolt. The orange fishing line can be seen attached to the eyebolt in the figure.

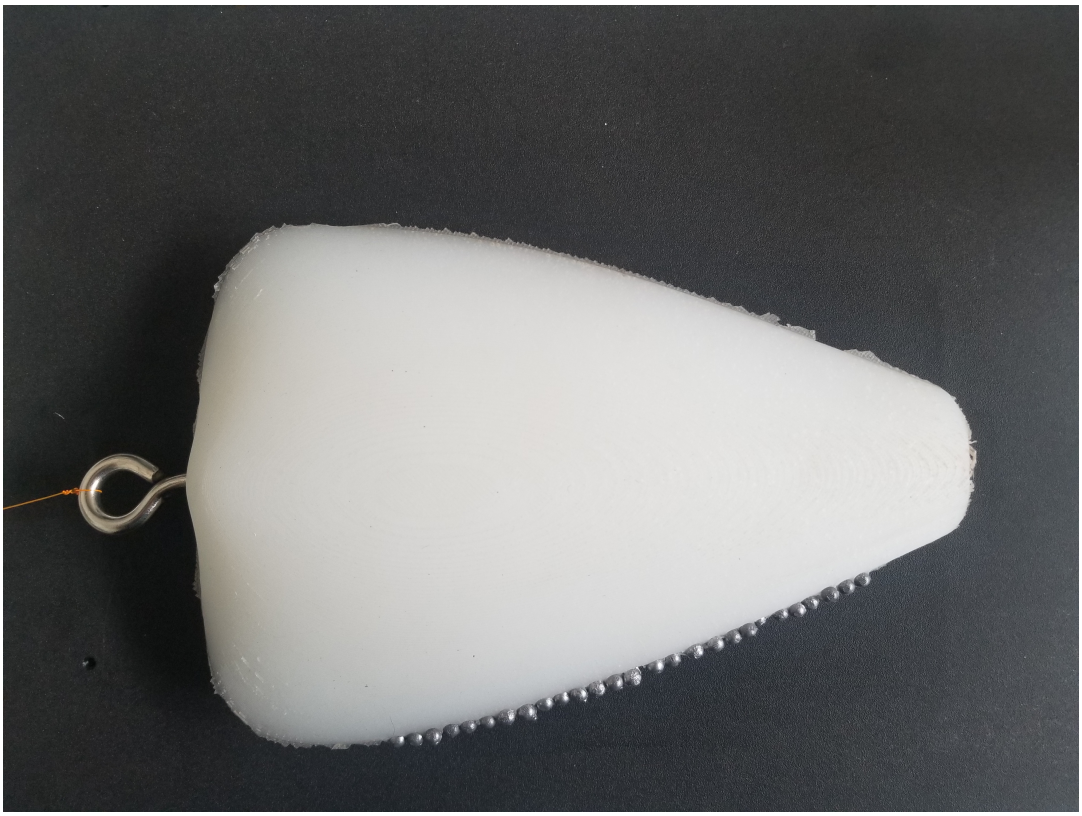

Figure 4.11. Cycle 5 free floating body with eyebolt and lead weights attached

For a submerged body to be stable in roll, its center of gravity must be below its center of buoyancy. Since the silicone rubber body had roughly a uniform density, the center of gravity and buoyancy coincided. Therefore, a number of small lead fishing weights were clamped to the bottom of the body to slightly lower the center of gravity and make the body stable in the roll axis. Unfortunately, this also caused the body to be quite negatively buoyant resulting in the body tending to drag along the bottom the water tunnel during testing.

4.5.4 Test

Changing the test set-up to allow six degrees-of-freedom motion introduced additional factors that had to be considered such as buoyancy and roll stability. During testing in

the water tunnel is was determined that the current body design was insufficient for wake synchronization as shown in Figure 4.12.

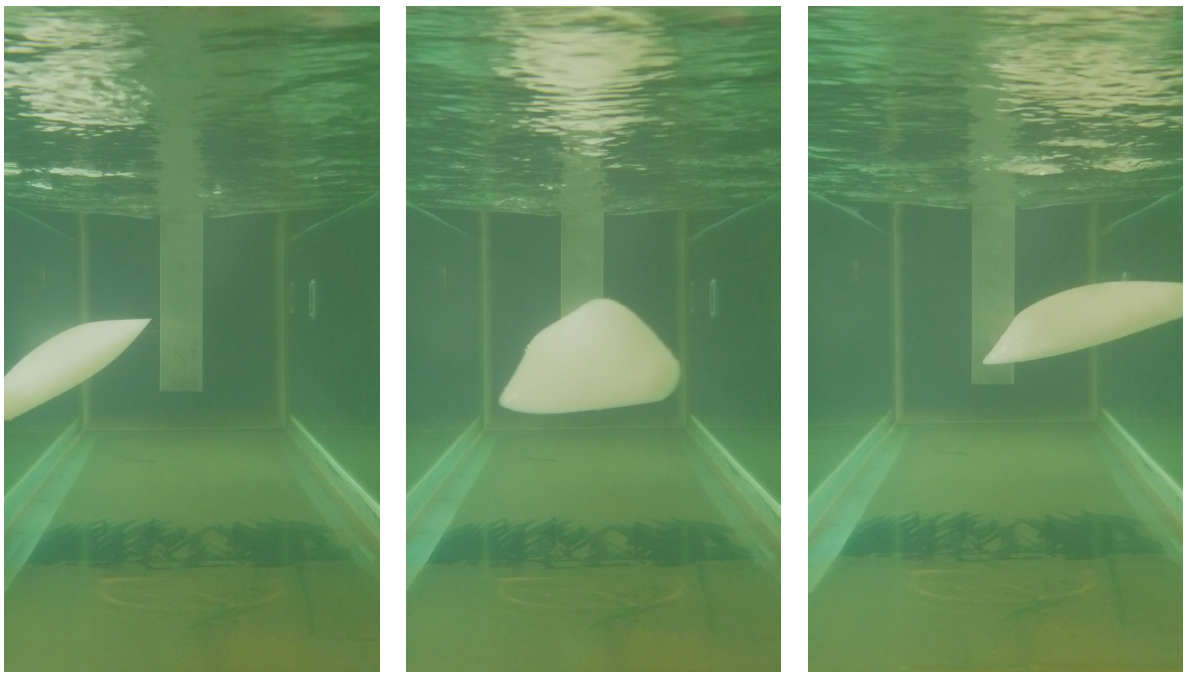

(a) Cycle 5 free floating body unweighted back view

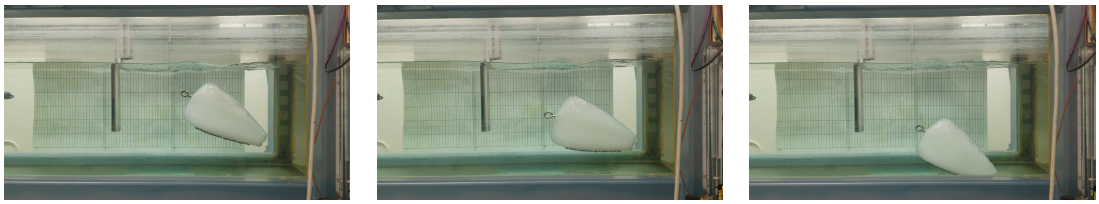

(b) Cycle 5 free floating body weighted side view

Figure 4.12. Cycle 5 free floating body performance with and without weight.

The body was observed to rotate 90 degrees and stabilize in the horizontal plane as seen in Figure 4.12(a). An encouraging observation was that the passing vortices has sufficient strength to displace and rotate the body. Adding additional lead weight to the bottom of the body did not remedy the stability problem and only made the body even more negatively buoyant as seen from the side view of the test section in Figure 4.12(b). The body shape needs to be updated so that it would be stable in the vertical plane while maintaining neutral

buoyancy. This could potentially be achieved by creating a hollow cavity within the body in future designs.

THIS PAGE INTENTIONALLY LEFT BLANK

CHAPTER 5:
Conclusion

This research effort was able to identify the important aspects for a flexible synthetic body to passively synchronizing with a vortex wake. First, the research proved that the silicone rubber material used in this study was sufficient to provide the required body flexibility to produce a flapping motion from the body. Second, a quick and inexpensive fabrication process for creating flexible bodies was demonstrated that can be repeated in future research efforts. Third, this research effort showed that direct fluid interaction with a flexible body is not likely to produce significant flapping motion. Finally, this investigation showed that the rotation of the forward part of a flexible body is a key factor to produce a flapping motion and passively synchronize within a vortex wake.

Future work on this research topic could explore various interactions observed during this investigation. Determining if rotational motion alone is sufficient, or if rotational motion needs to be coupled with translational motion, to generate thrust through passive synchronization requires further research that uses a free floating body and also a nearly friction-free rotational system. A nearly friction-free rotational test setup can be constructed using air bearings attached to a compressed air line. A test setup with both nearly friction-free rotational and translational degrees-of-freedom would be extremely difficult to create. However, this would allow further exploration of if lateral translational motion is required to produce flapping motion in a flexible synthetic body. If both rotation and translation is required, a free floating design is a reasonable way to explore this phenomenon. A free floating design is still complex because you need the center of gravity below the center of buoyancy. Unfortunately, a body molded with a uniform density silicon rubber will always have those two points being coincidental. The introduction of entrained air during the mixing process is also of concern and would require adding a vacuuming to the fabrication process. Future research could also explore body parameters that improve thrust generated from forced head rotation, especially focusing on if the tail should be reinforced with stiff "ribs" like a real fish. Finally, identification of the body parameters and their required values that improve flexible body stabilization within the vortex wake while attached to the D-Cylinder could be pursued.

THIS PAGE INTENTIONALLY LEFT BLANK

APPENDIX: Calibration Tables and Engineering Drawings

A.1 Load Cell Calibration

Table A.1. Calculated and measured load cell F_x calibration data with percent difference.

	Calculated F_x	Measured F_x	F_x Difference	Calculated M_y	Measured M_y	M_y Difference
Run	[lbs]	[lbs]	%	[in-lbs]	[in-lbs]	%
1	0.0472	0.0662	28.73	-0.17	-0.14937	12.85
2	0.1005	0.18688	46.21	-0.36	-0.49249	27.07
3	0.1470	0.23318	36.94	-0.53	-0.66275	20.72
4	0.2022	0.27085	25.36	-0.72	-0.84048	14.06
5	0.2491	0.29148	14.53	-0.89	-0.94626	5.93
6	0.3031	0.37094	18.28	-1.08	-1.1932	9.23
7	0.3499	0.35696	1.99	-1.25	-1.21626	2.78
8	0.3984	0.46453	14.24	-1.42	-1.53118	7.04
9	0.4511	0.49241	8.40	-1.61	-1.65447	2.59
10	0.50	0.58061	13.88	-1.79	-1.92309	7.10
11	1.00	1.05517	5.23	-3.57	-3.6826	2.98
12	1.50	1.56466	4.13	-5.36	-5.5091	2.72
13	2.00	2.04861	2.37	-7.15	-7.31721	2.34
14	2.50	2.50924	0.37	-8.93	-9.08666	1.70
15	3.00	3.03186	1.05	-10.72	-10.85834	1.28

Table A.2. Calculated and measured load cell F_y calibration data with percent difference.

	Calculated F_y	Measured F_y	F_y Difference	Calculated M_x	Measured M_x	M_x Difference
Run	[lbs]	[lbs]	%	[in-lbs]	[in-lbs]	%
16	0.0474	0.03517	34.77	0.17	0.07403	128.77
17	0.1014	0.09593	5.72	0.36	0.33699	7.52
18	0.1486	0.1436	3.48	0.53	0.52151	1.80
19	0.2019	0.19562	3.23	0.72	0.71765	0.54
20	0.2489	0.25246	1.41	0.89	0.98459	9.68
21	0.3038	0.28029	8.39	1.09	0.94283	15.13
22	0.3501	0.347	0.89	1.25	1.27745	2.08
23	0.3973	0.40181	1.13	1.42	1.55844	8.92
24	0.4517	0.43245	4.46	1.61	1.50052	7.56
25	0.50	0.4935	1.32	1.79	1.81059	1.33
26	1.00	0.98816	1.20	3.57	3.75887	4.94
27	1.50	1.48141	1.25	5.36	5.45431	1.74
28	2.00	1.97841	1.09	7.15	7.36055	2.91
29	2.50	2.47458	1.03	8.93	9.21546	3.07
30	3.00	2.95968	1.36	10.72	11.21098	4.39

A.2 Engineering Drawings

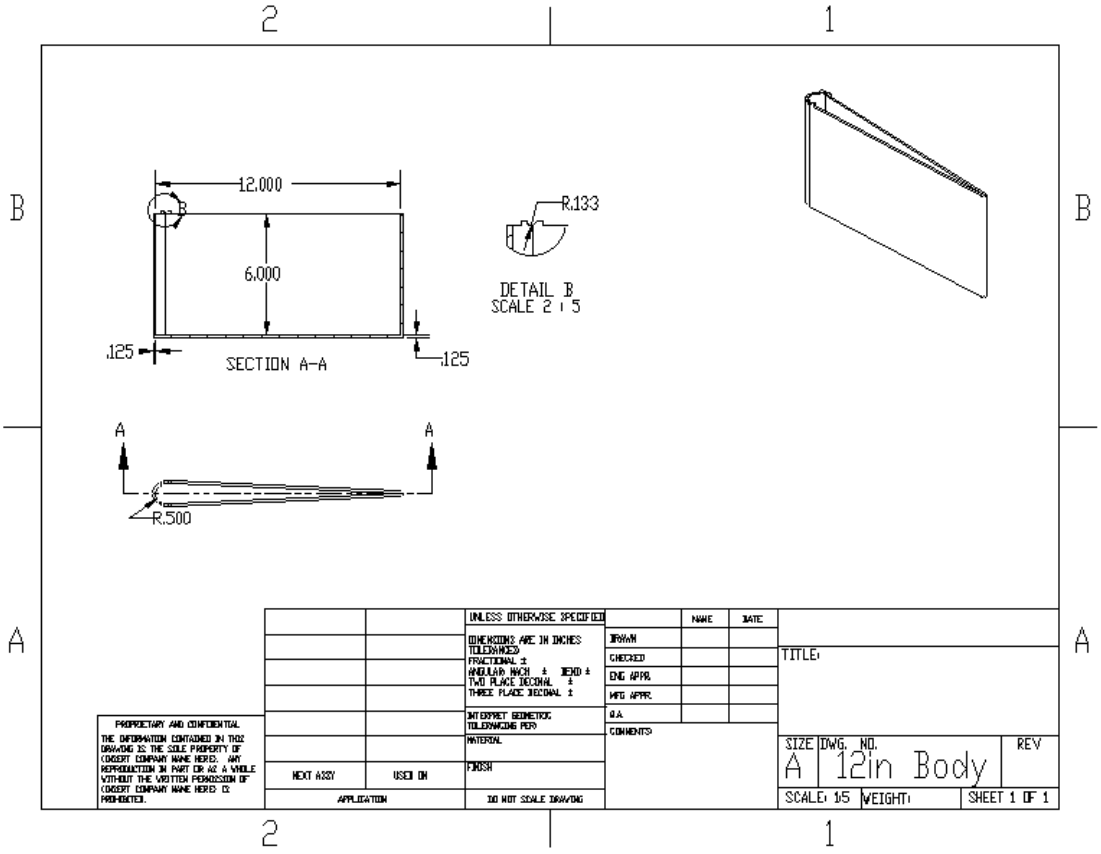

Figure A.1. Cycle 1 - 12in pennant body mold

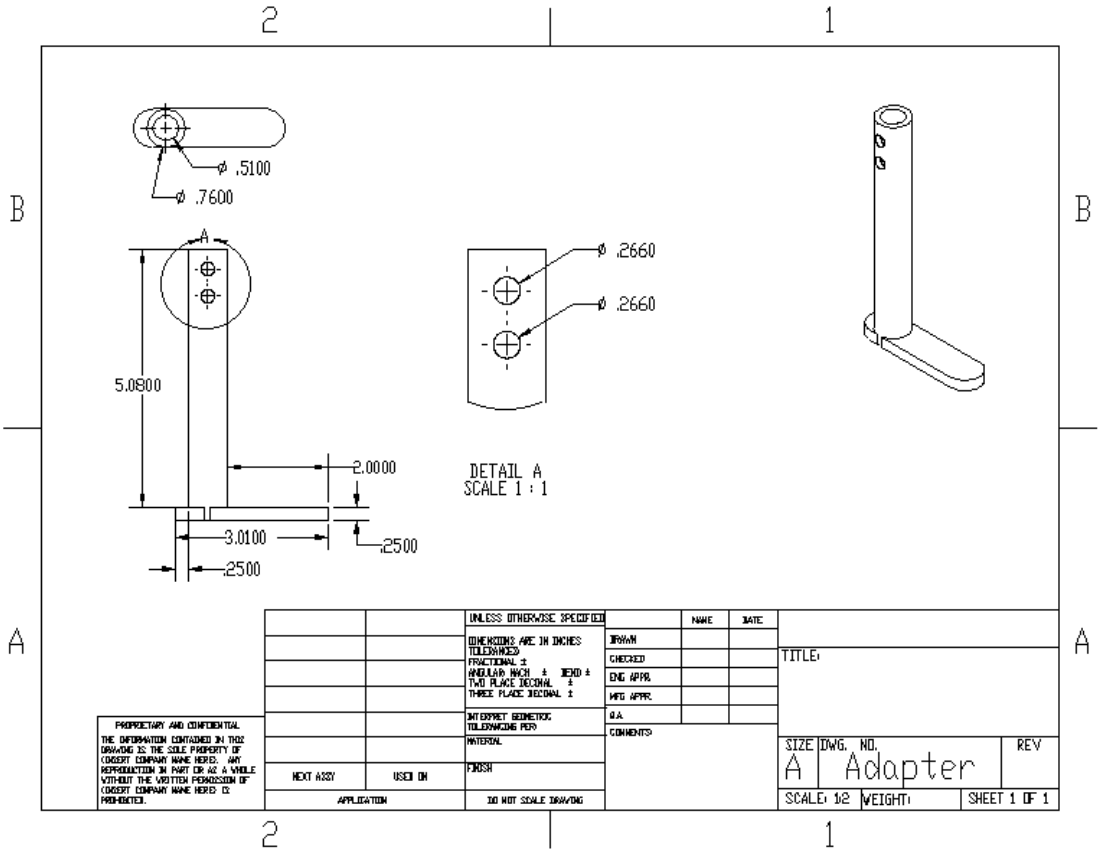

Figure A.2. Cycle 1 & 2 - 0.5in rod adapter

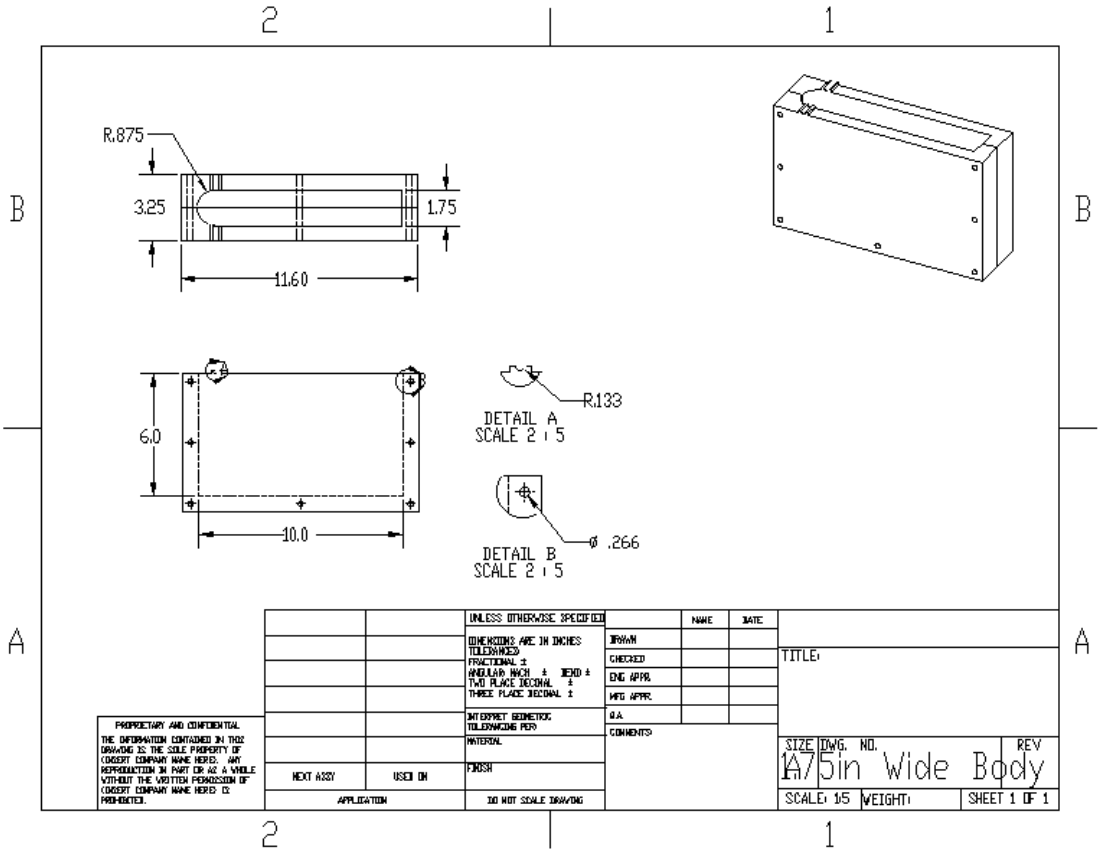

Figure A.3. Cycle 2 - 1.75in wide body

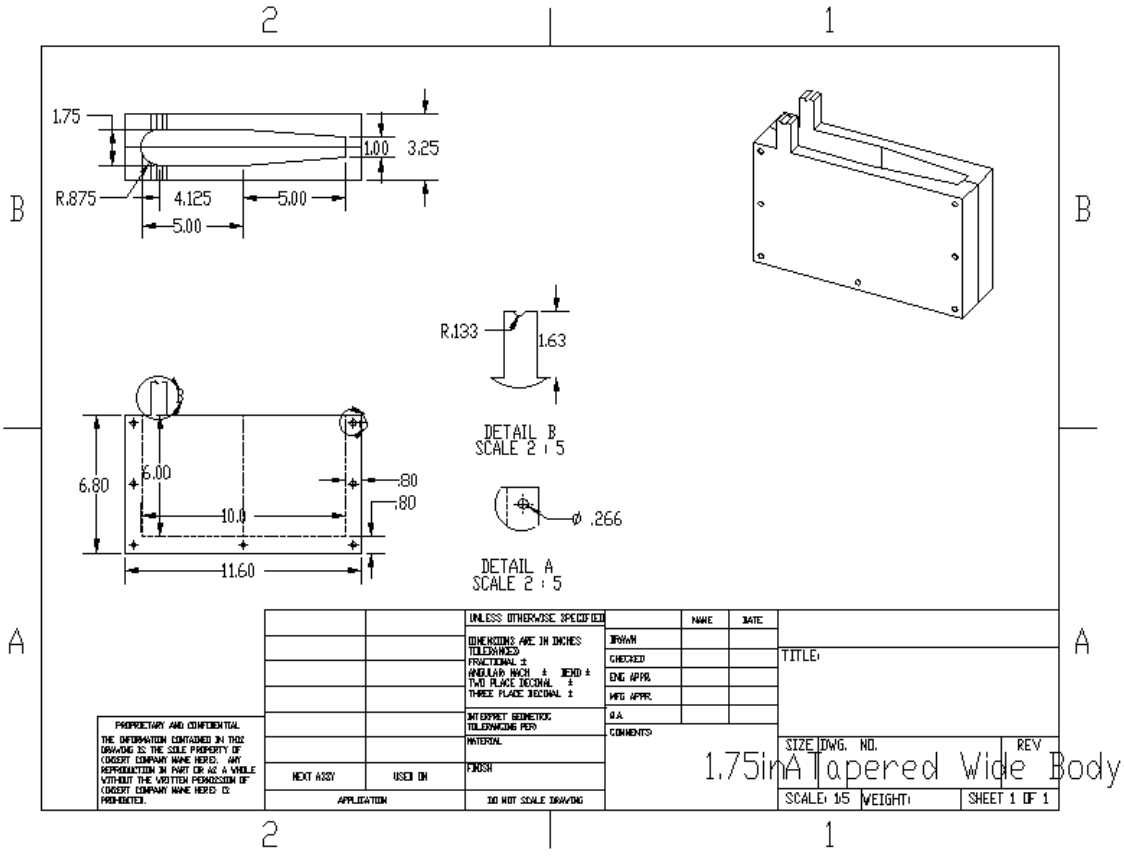

Figure A.4. Cycle 3 - 1.75in tapered wide body

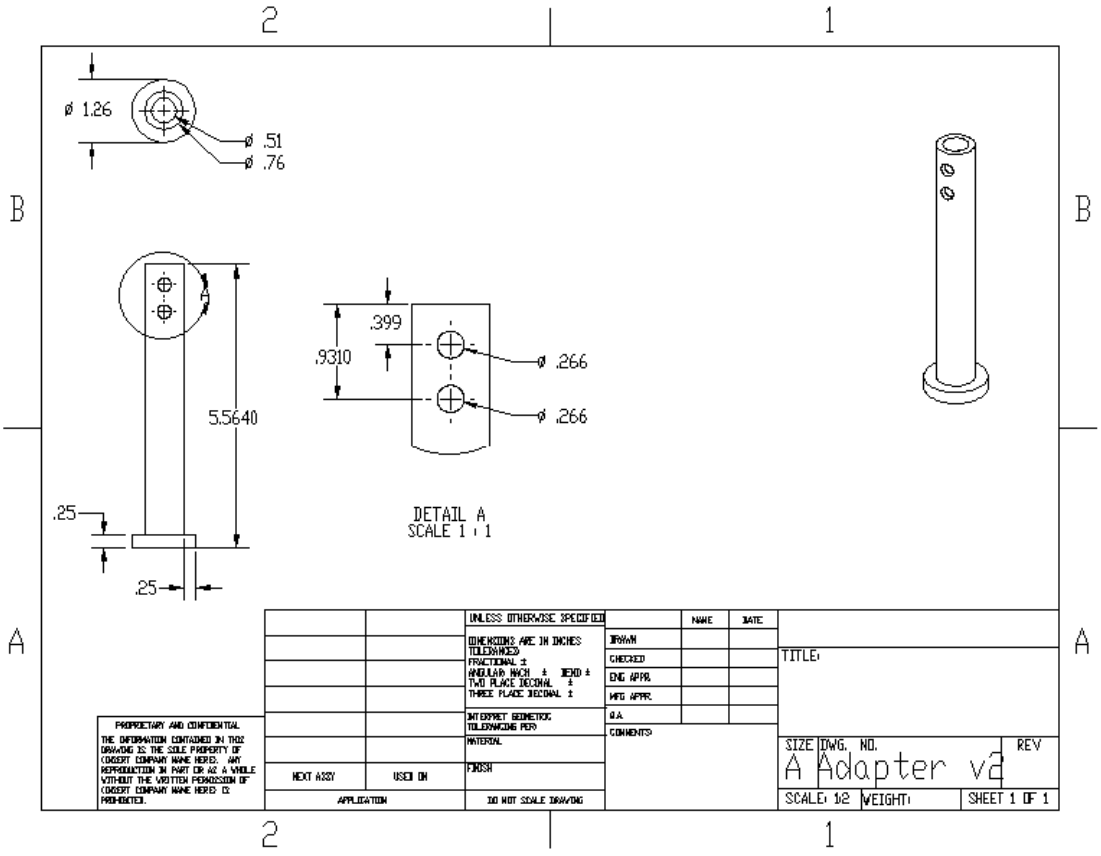

Figure A.5. Cycle 3 - internal rotational adapter

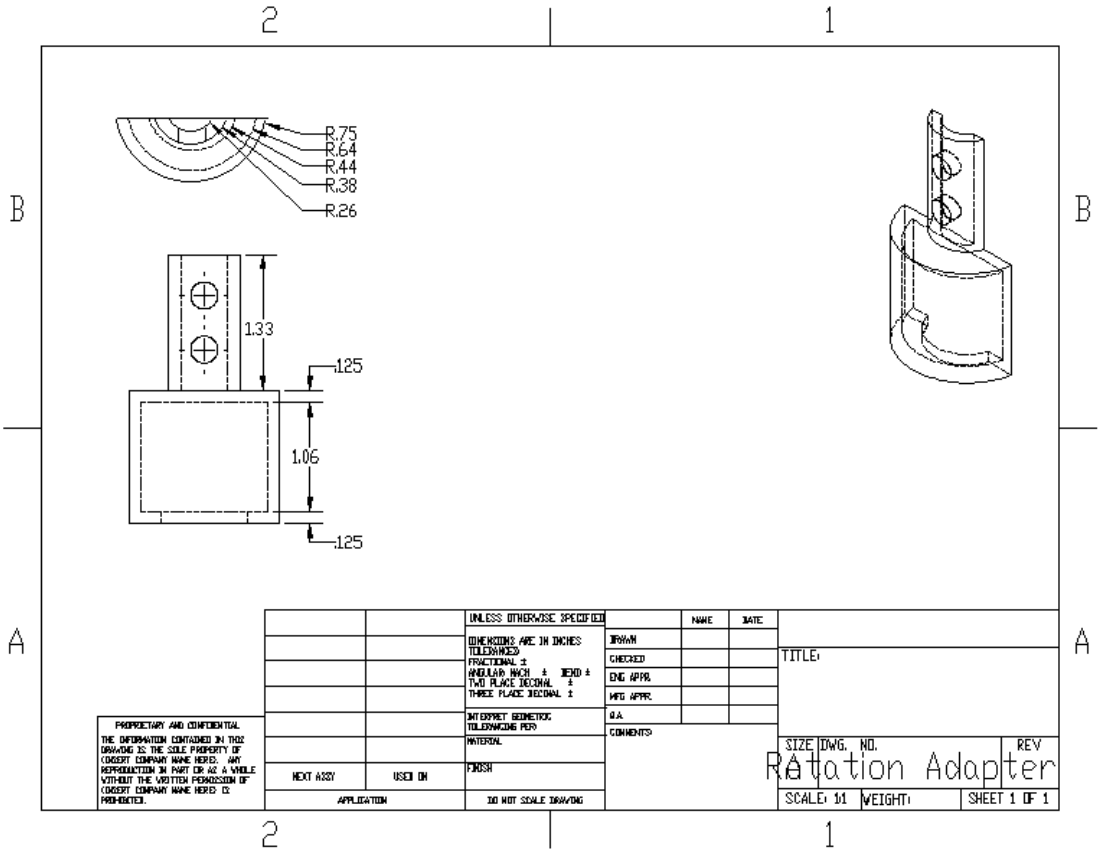

Figure A.6. Cycle 3 - external rotational insert

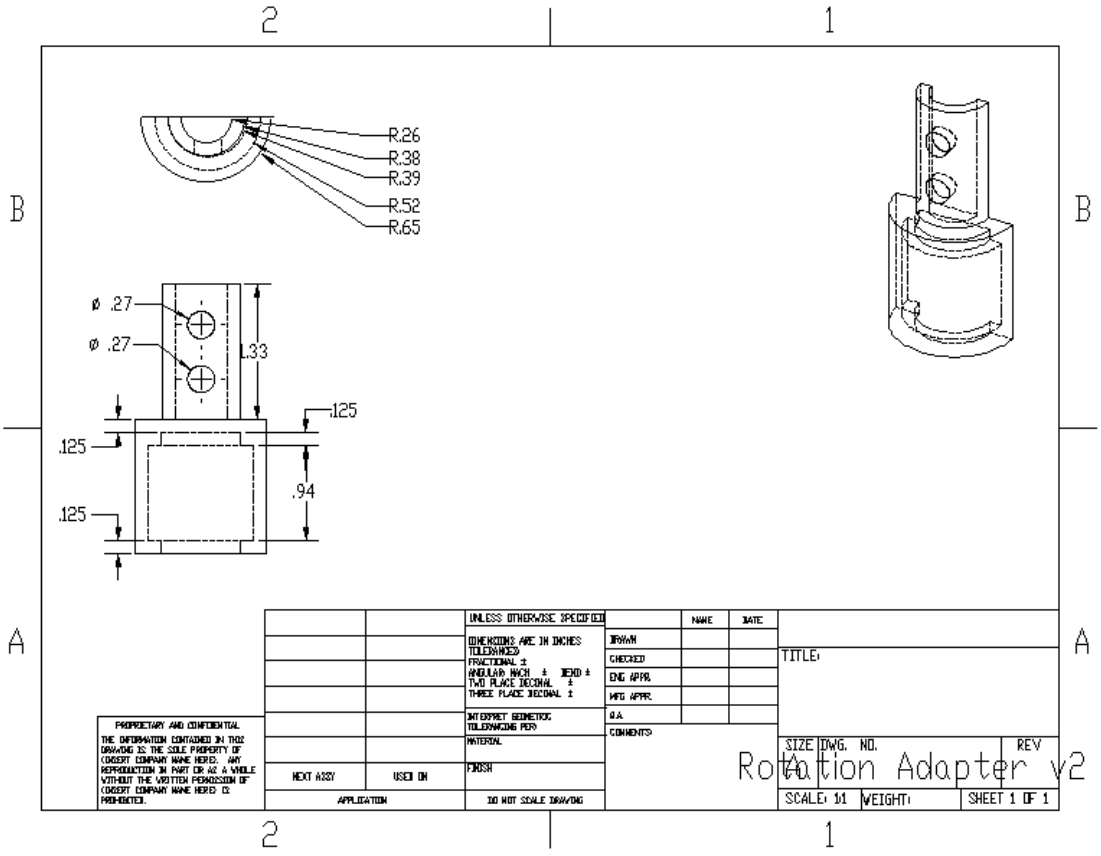

Figure A.7. Cycle 3 - external rotational insert fixed cant

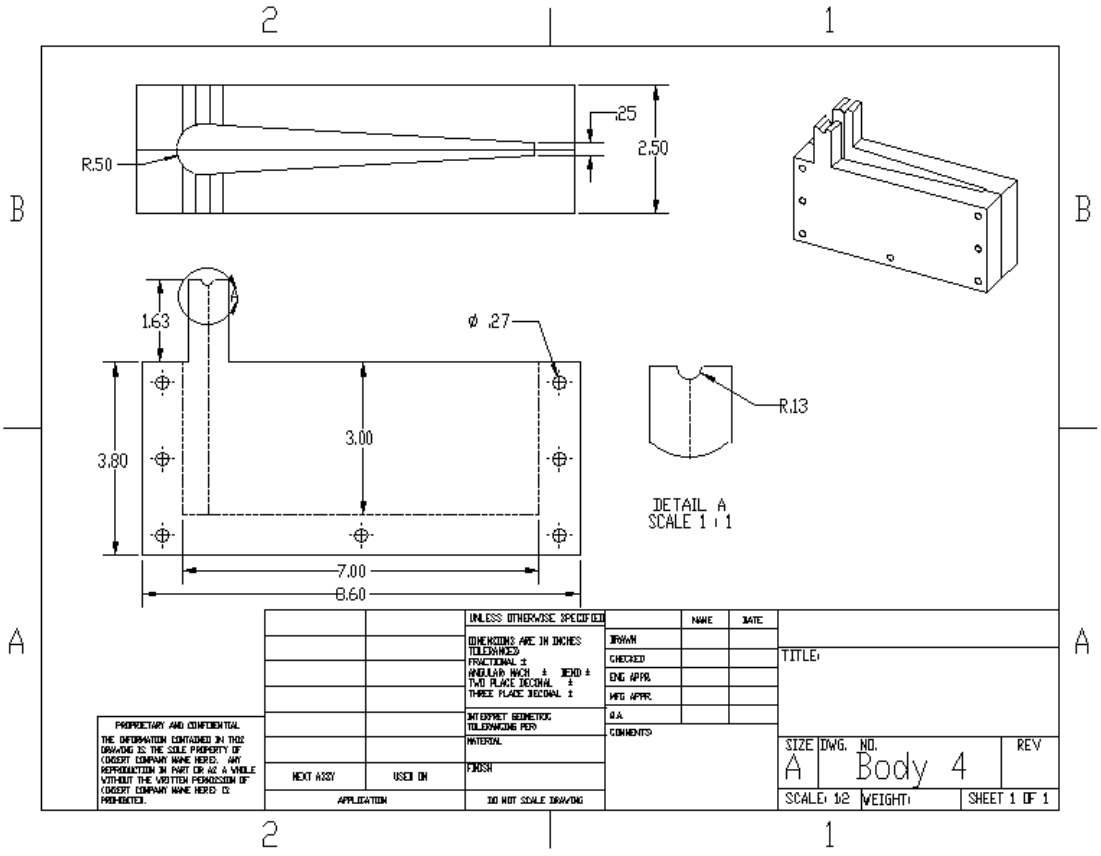

Figure A.8. Cycle 4 - forced motor body similar to Beal et al.

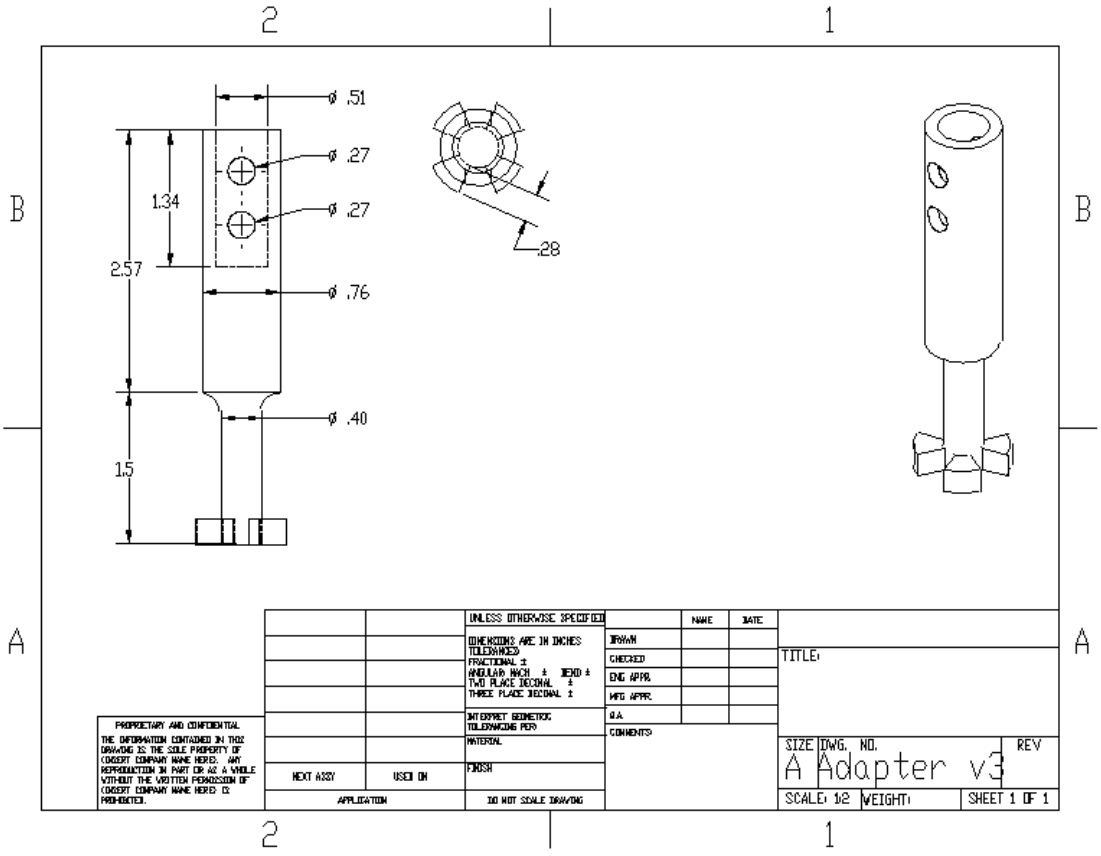

Figure A.9. Cycle 4 - propeller adapter

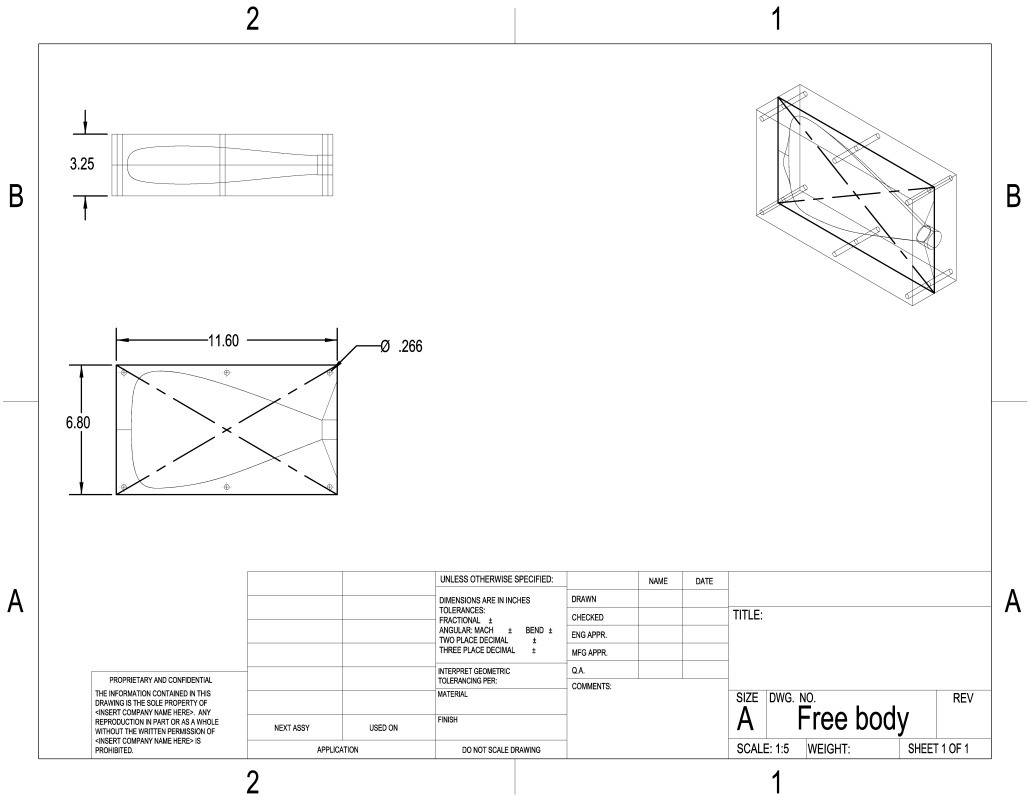

Figure A.10. Cycle 5 - free floating body

List of References

[1] B. Fletcher, "UUV master plan: a vision for navy UUV development," in *OCEANS 2000 MTS/IEEE Conference and Exhibition. Conference Proceedings (Cat. No. 00CH37158)*. IEEE, 2000, vol. 1, pp. 65–71.

[2] J. D. Lambert, P. Picarello, and J. E. Manley, "Development of UUV standards, an emerging trend," *OCEANS 2006*, pp. 1–5, 2006.

[3] The Engineering ToolBox (2004), "Strouhal number," July. 2023 [Online]. Available: https://www.engineeringtoolbox.com/strouhal-number-d_582.html

[4] The Engineering ToolBox (2003), "Reynolds number," July. 2023 [Online]. Available: https://www.engineeringtoolbox.com/reynolds-number-d_237.html

[5] R. A. Kumar, C.-H. Sohn, and B. H. Gowda, "Passive control of vortex-induced vibrations: an overview," *Recent patents on mechanical engineering*, vol. 1, no. 1, pp. 1–11, 2008.

[6] D. W. Olson, S. F. Wolf, and J. M. Hook, "The Tacoma Narrows bridge collapse," *Physics today*, vol. 68, no. 11, pp. 64–65, 2015.

[7] M. M. Bernitsas, K. Raghavan, Y. Ben-Simon, and E. Garcia, "VIVACE (vortex induced vibration aquatic clean energy): A new concept in generation of clean and renewable energy from fluid flow," *Journal of offshore mechanics and Arctic engineering*, vol. 130, no. 4, 2008.

[8] J. C. Liao, D. N. Beal, G. V. Lauder, and M. S. Triantafyllou, "Fish exploiting vortices decrease muscle activity," *Science*, vol. 302, no. 5650, pp. 1566–1569, 2003.

[9] D. N. Beal, F. S. Hover, M. S. Triantafyllou, J. C. Liao, and G. V. Lauder, "Passive propulsion in vortex wakes," *Journal of Fluid Mechanics*, vol. 549, pp. 385–402, 2006.

[10] G. Toming, L. D. Chambers, and M. Kruusmaa, "Experimental study of hydrodynamic forces acting on artificial fish in a von kármán vortex street," *Underwater Technology*, vol. 32, no. 2, pp. 81–91, 2014.

[11] O. Ruz, E. Castillo, M. Cruchaga, and A. Aguirre, "Numerical study of the effect of blockage ratio on the flow past one and two cylinders in tandem for different power-law fluids," *Applied Mathematical Modelling*, vol. 89, pp. 1640–1662, 2021. Available: https://www.sciencedirect.com/science/article/pii/S0307904X20304698

[12] Hanumanthu and K. V. Sreenivas Rao, "CFD study of solid wind tunnel wall effects on wing characteristics," *Indian Journal of Science and Technology*, vol. 9, 2016.

[13] G. M. Abbas, I. Gursel Dino, and M. Percin, "An integrated pipeline for building performance analysis: Daylighting, energy, natural ventilation, and airborne contaminant dispersion," *Journal of Building Engineering*, vol. 75, p. 106991, 06 2023.

[14] Racine Federated Inc., Racine, WI, USA, "Series tfxd transit time ultrasonic flow meter operations and maintenance manual," May. 2013 [Online]. Available: https://www.instrumart.com/assets/Dyna_TFXD_Manual.pdf

[15] ADVANCED MECHANICAL TECHNOLOGY, INC, Watertown, MA, USA, "MC3A force and torque sensor specification sheet," June. 2023 [Online]. Available: https://www.amti.jp/MC3A.pdf

[16] SMOOTH-ON Inc, "Durometer shore hardness scale," Jun. 2023 [Online]. Available: https://www.smooth-on.com/page/durometer-shore-hardness-scale/

[17] SMOOTH-ON Inc, "Ecoflex™ 00-10," Jun. 2023 [Online]. Available: https://www.smooth-on.com/products/ecoflex-00-10/

[18] Space Systems Academic Group at NPS, "3d printing home (3d geometry printed in plastic)," June. 2023 [Online]. Available: https://wiki.nps.edu/pages/viewpage.action?pageId=13107262

Initial Distribution List

1. Defense Technical Information Center
   Ft. Belvoir, Virginia

2. Dudley Knox Library
   Naval Postgraduate School
   Monterey, California